Εθνικό Μετσόβιο Πολυτεχνείο
Σχολή Μηχανολόγων Μηχανικών
Τομέας Ρευστών
Εργαστήριο Αεροδυναμικής

Ανάλυση της αεροδυναμικής αλληλεπίδρασης δρομέων τετραπτέρου

Διπλωματική εργασία

Συγγραφέας:
Ζιάβρας Χρήστος

Επιβλέπων Καθηγητής:
Ριζιώτης Βασίλειος, Αναπληρωτής Καθηγητής ΕΜΠ

Αθήνα 2023

National Technical University of Athens
School of Mechanical Engineering
Fluids Division
Laboratory of Aerodynamics

Analysis of the aerodynamic interactions of the rotors of a quadrotor

---

Diploma Thesis

Author:

Ziavras Christos

Supervisor:

Riziotis Vasilios, Associate Professor NTUA

Athens 2023

--- Blank page ---

Υπεύθυνη δήλωση για λογοκλοπή και για κλοπή πνευματικής ιδιοκτησίας:

Έχω διαβάσει και κατανοήσει τους κανόνες για τη λογοκλοπή και τον τρόπο σωστής αναφοράς των πηγών που περιέχονται στον οδηγό συγγραφής Διπλωματικών Εργασιών. Δηλώνω ότι, από όσα γνωρίζω, το περιεχόμενο της παρούσας Διπλωματικής Εργασίας είναι προϊόν δικής μου εργασίας και υπάρχουν αναφορές σε όλες τις πηγές που χρησιμοποίησα.

Οι απόψεις και τα συμπεράσματα που περιέχονται σε αυτή τη Διπλωματική εργασία είναι του συγγραφέα και δεν πρέπει να ερμηνευθεί ότι αντιπροσωπεύουν τις επίσημες θέσεις της Σχολής Μηχανολόγων Μηχανικών ή του Εθνικού Μετσόβιου Πολυτεχνείου.

Ζιάβρας Χρήστος

Acknowledgements

I would like to express my deepest gratitude to everyone who has supported me throughout my academic journey. First and foremost, I would like to thank my family for their love, encouragement, and belief in me. Their sacrifices and unwavering support have been instrumental in helping me achieve this milestone.

I also want to express my appreciation to my professors and mostly Prof. Riziotis, who have challenged me, taught me, and inspired me to think critically and creatively. Their guidance and expertise have been invaluable, and I am grateful for their contribution to my education.

I would like to thank my classmates for the countless hours of study sessions and to apologize to my friends for the countless missed gatherings. Your friendship and support have made this journey enjoyable and memorable.

Lastly, I would like to thank the administration of NTUA for creating an environment conducive to learning and growth and everyone else who has contributed to my success. I am proud of this achievement and look forward to the opportunities it will reveal.

Table of Contents

1. Σύνοψη 7
2. Abstract 8
3. Acronyms 9
4. Table of figures 10
5. Introduction 12
   5.1 Scope 14
   5.2 Delimitation 14
   5.3 Literature Review 17
6. Methodology 22
   6.1.1 Experimental Set-up 22
   6.1.2 Computational Methods - CORAL 24
   6.1.3 Noise Emissions 27
   6.1.4 Configurations 27
   6.1.5 PIV Measurements 28
7. Results 29
   7.1 General Overview 29
   7.2 Experimental Data 29
   7.3 Computational Results 30
      7.3.1 Square Configurations 30
      7.3.2 Diamond Configuration 31
   7.4 Experimental Data & Computational Results 32
      7.4.1 Bearhug 32
      7.4.2 Breaststroke 32
      7.4.3 Diamond 33
   7.5 Overall Efficiency & Power 40
   7.6 PIV Measurements 41
      7.6.1 Front rotors – Bearhug 41
      7.6.2 Aft rotors - Bearhug 42
      7.6.3 General Overview - Bearhug 43
      7.6.4 General Overview – Diamond 48
8. Discussion 53
9. Conclusions 57
10. Appendix 59
   10.1 I. CORAL code 59
11. References 60

1. Σύνοψη

Η εν λόγω διπλωματική εργασία παρουσιάζει μέρος των αποτελεσμάτων της αυτοχρηματοδοτούμενης έρευνας “Αεροδυναμική Αλληλεπίδραση δρομέων” του δικτύου AG-25 του οργανισμού GARTEUR. Η έρευνα που διεξήχθη πραγματεύεται την αλληλεπίδραση της ροής μεταξύ τεσσάρων ταχέων δρομέων ενός τετράπτερου σε χιαστί και σταυρωτή διάταξη με παράλληλη εναλλαγή των αποστάσεών τους. Κάθε ίδρυμα που εντάσσεται στο δίκτυο AG-25 μοντελοποίησε την πειραματική διάταξη αναφοράς με χρήση εσωτερικά (IN-HOUSE) ανεπτυγμένου λογισμικού και καινοτόμες παραδοχές. Σκοπός είναι η σύγκριση των αποτελεσμάτων μεταξύ των διαφόρων πανεπιστημίων και η ανάδειξη των πλεονεκτημάτων και μειονεκτημάτων των μεθόδων που εφαρμόστηκαν. Η μοντελοποίηση του πειράματος αναφοράς, που διεξήχθη από το ερευνητικό κέντρο DLR, ξεκίνησε με την χρήση του Μέσης Πιστότητας (Medium-Fidelity) κώδικα CORAL, όπου το αεροδυναμικό μέρος είναι δημιούργημα του Εθνικού Μετσόβιου Πολυτεχνείου, και συγκεκριμένα με τη μέθοδο της γραμμής άνωσης. Σε εκείνη κάθε τομή του πτερυγίου έχει μόνο δύο κόμβους, οι οποίοι αντιπροσωπεύουν την ακμή πρόσπτωσης και εκφυγής αντίστοιχα. Ουσιαστικά, η αεροτομή μετουσιώνεται σε επίπεδη πτέρυγα. Στην συνέχεια, τα αποτελέσματα συγκρίθηκαν με εκείνα της επιφάνειας άνωσης και της τριδιάστατης μεθόδου συνοριακών στοιχείων (3D panel). Στην λεπτή επιφάνεια άνωσης οι κόμβοι ανά τομή είναι περισσότεροι από δύο και αναπαράγουν την μέση καμπυλότητα της αεροτομής δημιουργώντας μια καμπύλη πτέρυγα, ενώ στο τρισδιάστατο σώμα διαμορφώνεται επακριβώς το σχήμα της αεροτομής. Η τελική αξιολόγηση των τετράγωνων διατάξεων, bearhug και breaststroke, ανέδειξε ότι η ευθυγράμμιση των πρόσθιων ρότορων δίπλα-δίπλα (Side-by-Side) είναι απίστευτα ευεργετική. Ωστόσο, η ευθυγράμμιση μεταξύ των πρόσθιων και των πίσω ρότορων (τύπου Tandem) είχε έντονο αρνητικό αντίκτυπο στους πίσω ρότορες, καθώς αυτοί λειτουργούσαν εντός της κατακόρυφης ροής αέρα (downwash) που δημιουργούν οι πρόσθιοι. Παρόλα αυτά, ενθαρρυντικά αποτελέσματα προσέδωσαν οι αποστάσεις των ρότορων με ελαφρώς επικαλυπτόμενα πτερύγια, καθώς δεν ενίσχυαν μόνο την απόδοση των πρόσθιων ροτόρων όπως προαναφέρθηκε, αλλά επίσης επηρεάζαν θετικά τους πίσω ρότορες μέσω των παραγόμενων πλευρικών αλληλεπιδράσεων που δημιουργούσαν. Επιπλέον, τα πιο ενδιαφέροντα αποτελέσματα παρατηρήθηκαν για την διάταξη diamond. Για όλες τις μη επικαλυπτόμενες αποστάσεις των πτερυγίων, η συνολική παραγόμενη ώση της διάταξης ήταν μεγαλύτερη και η απαιτούμενη ισχύς ήταν μικρότερη από την περίπτωση των τεσσάρων ανεξάρτητων ρότορων. Το φαινόμενο αποδίδεται στη λειτουργία των πλευρικών δρομέων εντός της περιοχής ανόδου (upwash) που δημιουργούν οι αναδιπλούμενοι στρόβιλοι του ακροπτερυγίου (rolled-up tip vortices) στον πρώτο ρότορα. Συνολικά, τα αποτελέσματα είχαν πολύ μικρή απόκλιση από τα πειραματικά δεδομένα για όλες τις δοκιμές σε αρνητική κλίση πτήσης. Για θετική κλίση, οι γενικές μορφές (trends) των καμπυλών της ροπής ήταν επίσης ακριβείς, αλλά υπήρξε σημαντική απόκλιση στο μέτρο τους. Τέλος, τα παραπάνω ευρήματα της διπλωματικής δύνανται να είναι χρήσιμα για την βιομηχανία κατασκευής ταχέων πολυπτέρων, η οποία πάσχει από την απουσία εμπεριστατωμένης έρευνας αναφορικά με την οδηγικά βέλτιστη διάταξη και την απόσταση των δρομέων.

2. Abstract

This thesis presents the results of a self-funded research project called “Analysis of the aerodynamic interactions of the rotors of a quadrotor” initiated by the AG-25 group of the GARTUER framework. The main topic of this research is the investigation of the interactions between four high-speed rotors in a plus or a cross configuration, while alternating their rotor spacing. Vital role for the simulation of the stated configurations played the Medium-Fidelity CORAL software, whose aerodynamic code was developed by the fluids’ division of NTUA. Each institute that participated in the AG-25 group modeled the reference experiment with the use of an IN-HOUSE developed software and had the ability to set any partial boundary or initial conditions that would enhance the accuracy of the results. The aim of this project was the comparison of every software’s results and the acknowledgement of the best for the simulation of the flow. The reference experiment, that was conducted by the research center DLR, was initially reproduced by CORAL through the use of the lifting line method (L.L.). In L.L., each section had only two nodes describing the leading and trailing edge points of the airfoil, which therefore rendered it into a flat plate. Afterwards, the methods lifting surface (L.S.) and thick body panel method (T.B.) were utilized. At L.S. method each section had more than two nodes that shaped the mean curvature line of the airfoil, while at the T.B. method the nodes produced the exact shape of the airfoil. The final assessment of the square test cases, bearhug and breaststroke, revealed that the alignment of the front rotors in Side-by-Side configuration was extremely beneficial. However, the Tandem configuration among the front and the aft rotors had a significantly negative impact on the aft rotors, as they operated within the downwash generated by the front. Nonetheless, rotor hub distances with slightly overlapping blades presented the highest efficiency compared to the rest. Not only was the performance of the front rotors enhanced, but also the aft rotors were positively influenced by the side-by-side interactions that these kinds of distances generated. Additionally, the most noteworthy results were calculated for the diamond test case. For all its non-overlapping hub distances the diamond’s total output thrust was higher and the required power was less than those of four single rotors. The main incendiary was the operation of the lateral rotors within the first rotor’s upwash regions, which were formed by its rolled-up tip vortices. Overall, the computational results demonstrated good agreement with the measured data for all the test cases at a negative rotor plane tilt. For a positive rotor plane tilt, the trends were also accurate, but there was a noticeable level difference in the magnitude of the numerical torque calculations. In conclusion, the presented research findings can be useful for the high-speed multicopter industry, since it lacks of solid research on optimized quadrotor configurations and rotors’ spacing.

3. Acronyms

AG	Action Group
BEM	Blade Element Momentum
BOS	Background-oriented Schlieren
BSL	Menter Baseline Model
CFD	Computational Fluid Dynamics
CORAL	Comprehensive Rotorcraft Analyses Lab
CPU	Central Processing Unit
D	Diameter of the KDE 12.5x4.3"
d	Relative rotor distance
DLR	Deutsches Zentrum für Luft und Raumfahrt
GARTEUR	Group for Aeronautical Research and Technology in Europe
IAG	University of Stuttgart
L.L.	Lifting Line
L.S.	Lifting Surface
MEMS	Micro-electro-mechanical systems
NACA	National Advisory Committee for Aeronautics
NTUA	National Technical University of Athens
PIV	Particle Image Velocimetry
PoliMi	Politecnico di Miliano
RANS	Reynolds Averaged Navier
Re	Reynolds Number
RPM	Rounds Per Minute
RSM	Reynolds stress equation model
RTG	Rotor Test Stand
SPIV	Stereo Particle Image Velocimetry
SST	Shear Stress Transport
T.B.	Thick Body
UAV	Unmanned aerial vehicle
UPM	Unsteady Panel Methods
VP	Vortex Particle
VTOL	Vertical take-off and landing

4. Table of figures

Figure 1: Bell UH-1 Iroquois (Wikipedia). 12
Figure 2: Karman K-max (Wikipedia). 12
Figure 3: Sikorsky S-97 Raider (Wikipedia). 13
Figure 4: Animation of Rotor-Rotor interactions (A. Kostek, 2022). 14
Figure 5: ONERA test rig mounted in the L2 Wind-Tunnel (R. Boisard et al., 2022). 15
Figure 6: PoliMi full rig, wind tunnel configuration for testing (R. Boisard et al., 2022). 15
Figure 7: DLR, experimental multicopter setup (R. Boisard et al., 2022). 16
Figure 8: Regions of flow - Rotor in ground effect (M. Ramasamy et al., 2015). 17
Figure 9: The three different configurations, (1) conventional configuration, (2) coaxial configuration, (3) new configuration (He Zhu et al., 2020). 19
Figure 10: Non-interactive High Re wake & Interactive Low Re wake (D. Shukla et al., 2018). 19
Figure 11: Side-by-side, Tandem & Oblique Configurations (Anna A. Kostek, 2023). 21
Figure 12: Flow chart of the DLR's experimental proceedings. 22
Figure 13: Experimental setup in RTG (R. Boisard et al., 2022). 23
Figure 14: Types of propellers - KDE 12.5x4.3" & Aeronaut CAM- Carb. Light 12x4.5" (A. Kostek, 2022). 23
Figure 15: CORAL's computational blocks for the L.L, L.S., T.B. (V. Riziotis et al., 2019) 24
Figure 16: Conversion of the wake filaments into vortex particles (V. Riziotis et al., 2019). 25
Figure 17: Plus and cross configurations (A. Kostek, 2022). 27
Figure 18: Test cases, relative distances and relative phasing of the propellers (R. Boisard et al. 2022). 27
Figure 19: The two studied tilt angles -10° & +10° (Anna A. Kostek, 2023). 28
Figure 20: Relative distances for the plus and cross configurations. 28
Figure 21: PIV measurements – Induced velocity distribution (A. Kostek, 2022). 28
Figure 22: Bearhug Configuration – Plane tilt -10° – Potential & Viscous. 34
Figure 23: Bearhug Configuration – Plane tilt +10° – Potential & Viscous. 35
Figure 24: Breaststroke Configuration – Plane tilt -10° – Potential & Viscous. 36
Figure 25: Breaststroke Configuration – Plane tilt +10° – Potential & Viscous. 37
Figure 26: Diamond Configuration – Plane tilt -10° – Potential & Viscous. 38
Figure 27: Diamond Configuration – Plane tilt +10° – Potential & Viscous. 39
Figure 28: Change in the system's overall mean Thrust & Torque for every test case. 41
Figure 29: PIV - Velocity field of the front rotors for increasing hub distances. 42
Figure 30: PIV – Velocity field of the downwash region among the front rotors for intense overlapping, slight overlapping & no overlapping. 42
Figure 31: PIV - Velocity field of the quadrotor for increasing d/D. 43
Figure 32: PIV - Velocity field of the quadrotor for d/D=0.74. 44
Figure 33: PIV - Velocity field of the quadrotor for d/D=0.84. 44
Figure 34: PIV - Velocity field of the quadrotor for d/D=0.96. 45
Figure 35: PIV - Velocity field of the quadrotor for d/D=1. 45
Figure 36: PIV - Velocity field of the quadrotor for d/D=1.22. 46

Figure 37: PIV - Velocity field of the quadrotor for d/D=1.44. 46
Figure 38: PIV - Velocity field of the quadrotor for d/D=1.7. 47
Figure 39: PIV - Velocity field of the diamond test case for increasing d/D. 48
Figure 40: PIV - Velocity field of the diamond test case for d/D=0.74. 49
Figure 41: PIV - Velocity field of the diamond test case for d/D=0.84. 49
Figure 42: PIV - Velocity field of the diamond test case for d/D=0.96. 50
Figure 43: PIV - Velocity field of the diamond test case for d/D=1. 50
Figure 44: PIV - Velocity field of the diamond test case for d/D=1.22. 51
Figure 45: PIV - Velocity field of the diamond test case for d/D=1.44. 51
Figure 46: PIV - Velocity field of the diamond test case for d/D=1.7. 52
Figure 47: Research Results – Bearhug Configuration – Plane tilt -10°/+10°. 54
Figure 48: Research Results – Breaststroke Configuration – Plane tilt -10°/+10°. 55
Figure 49: Research Results – Diamond Configuration – Plane tilt -10°/+10°. 56

5. Introduction

Generally, the design process of a conventional helicopter involves two rotors that rotate in various configurations. These configurations usually consist of main & tail rotors [1] (Figure 1) or side-by-side rotors [2] (Figure 2). However, there are a few different key points for the design of high-speed helicopters (Figure 3). First of all, the main rotor cannot be used as a high-speed propulsive mean since it is not able to reach high enough thrust values to provide both the necessary lift and driving force. In case that high cruising speed, a propeller is essential in order to achieve high advancing velocities.

Figure 1: Bell UH-1 Iroquois (Wikipedia).

Figure 2: Karman K-max (Wikipedia).

Figure 3: Sikorsky S-97 Raider (Wikipedia).

The interaction between the wakes of two rotors that rotate in different planes increases the complexity of the aerodynamic calculations. Chances are that noise levels, vibrations and unsteadiness deteriorate while the rotation planes of the rotor and the propeller diverge, thus a numerical approach of the problem through high order aerodynamic computational tools may seem inevitable. Except for that, the simulation of the wakes has to be accurate over long distances which increases further the computational cost. Also, the flow tends to be unsteady at low speeds and needs to be averaged over a specific period of time. Free wake or Low order models should be developed in this case that require adequate experimental databases setting another hindrance against a rational computational cost.

The action group AG-25 was created with the aim of addressing these problems. Its members are three research centers: ONERA (France), CIRA (Italy), DLR (Germany), and four universities: Politecnico di Miliano (PoliMi) (Italy), University of Glasgow (UoG) (United Kingdom), National Technical University of Athens (NTUA) (Greece) and University of Stuttgart (IAG) (Germany). All these institutes have to gather a database that will shed light upon numerical and experimental rotor-propeller wake interactions on high-speed rotors that operate at low-speed conditions. This thesis represents a proportion of Greece's contribution to this giant effort.

5.1 Scope

As stated above the incentive of this paper is the absence of literature about interactions between rotating parts of high-speed and multi-rotor rotorcraft concepts. The prosecution of numerous experiments will enable the creation of experimental databases that will improve the understanding of rotor-rotor interactional physics (Figure 4). Subsequently, the presented research can be very important for avian vehicles' performance and stability, all the more nowadays that products like drones are getting vastly popular. The ultimate long-term goal, however, is the increase but also the improvement of the worldwide numerical methods that are implemented for the simulation of multirotor interactions.

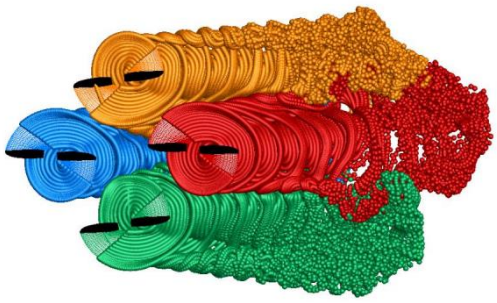

Figure 4: Animation of Rotor-Rotor interactions (A. Kostek, 2022).

5.2 Delimitation

The AG-25 group created three experiments that were complementary to each other and took place in various wind tunnels Europewide [3]:

The first experiment was conducted at ONERA (Figure 5). The ONERA experiment was centered around the studying of aerodynamic interactions that occur on fast rotorcraft designs, such as the X3 or RACER models manufactured by Airbus Helicopters [4]. A scaled-down helicopter model, specifically the DAUPHIN 365 N at a 1/77 scale, was utilized with a small four bladed propeller. This model was equipped with a fully articulated four-bladed rotor, completed with collective and cyclic pitch controls, and had a rotor radius of 0.75m, a nominal rpm of 1270, and a rotor tip speed of approximately 100m/s. The four-bladed propeller was manufactured by the APC company (APC11x9-4) with a diameter of approximately 28cm (11 inches). The ONERA L2 largesize low-speed wind tunnel was used as the testing environment. It is an open-circuit wind tunnel featuring a closed test section with a width of 6m, a height of 2.4m, and a length of 13m. The experiment's main parameter was the variation of the wind speed between 0 $m.s^{-1}$ and 19 $m.s^{-1}$, while measurements were obtained using two six-axis balances (one for the main rotor and one for the propeller), as well as accelerometers and angle sensors of the rotors' blades pitch, yaw, and lag.

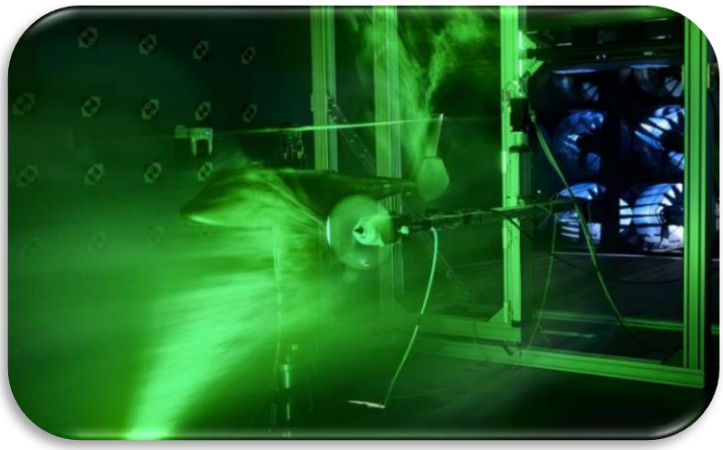

Figure 5: ONERA test rig mounted in the L2 Wind-Tunnel (R. Boisard et al., 2022).

The second experiment was conducted at PoliMi (Figure 6). The experimental setup wind-tunnel test rig included a fully-articulated, five-bladed main rotor mounted on a whirl tower, which was equipped with rectangular and untwisted NACA 0012 blades [3]. Additionally, there were two five-bladed side propellers, which were manufactured by varioPROP, both right- and left-handed. The main rotor had a radius of 0.855m and was fitted with sensors to measure the blades' pitch, flap, and lag angles, as well as a load cell to measure the rotor's loads. Each propeller had a radius of 0.15m and was powered by a Skorpion electric motor. They were arranged in a pusher configuration, which is similar to the design used in recent high-speed rotorcrafts like the RACER. A Futek load cell was connected to each propeller to measure the thrust and torque generated.

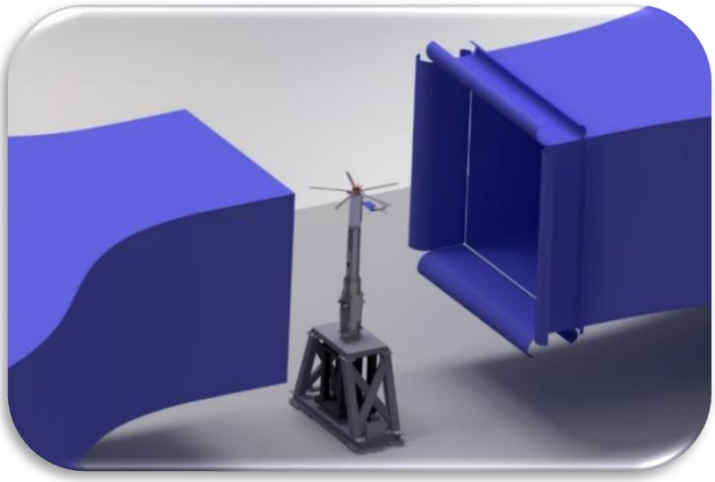

Figure 6: PoliMi full rig, wind tunnel configuration for testing (R. Boisard et al., 2022).

The last experiment was conducted at DRL (Figure 7) with the intent of exploring the aerodynamics and aeroacoustics of small rotor blades and their corresponding rotor-rotor interactions [3]. The DLR's rotor test stand Göttingen (RTG) was an Eiffel-type wind tunnel with an open test section. To achieve flow velocities of up to 23m/s, a nozzle outlet of 1.6m x 0.8m was selected for the measurements. Two- and three-bladed rotors with diameters ranging from 30.5cm to 62.2cm were mounted vertically in the test section on a rotatable support system that allowed for rotor tilt angle variations between -30° and 30°. A 180W brushless DC motor powered the rotor. Also, load sensors were installed in the drive unit to measure thrust and torque. To visualize tip vortices in the rotor wake, a background-oriented Schlieren (BOS) setup was used. The rotor's noise emissions were measured using an innovative microphone array, consisted of 512 micro-electro-mechanical systems (MEMS) microphones. Aside from the single rotor investigation, the final testing included the study of various multicopter configurations of up to four rotors that could be controlled in phase. The multicopter experiments involved in the variation of the relative distances between the multicopter's rotors while they were placed in plus and cross configurations.

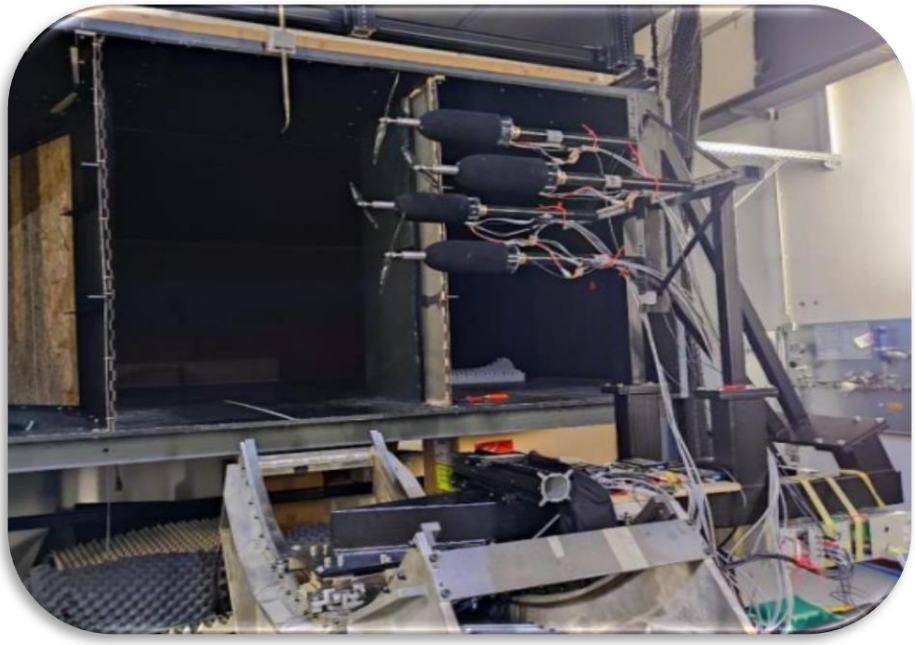

Figure 7: DLR, experimental multicopter setup (R. Boisard et al., 2022).

In this thesis only the third experiment has been further analyzed as the first two were excluded. Additionally, the experimental data that were acquired by the DLR validated the accuracy of the in-house code CORAL, developed by National Technical University of Athens (NTUA), for the case of a quadrotor with four two bladed rotors.

5.3 Literature Review

In this chapter useful citations are reviewed. At first, some general information is presented about flow interactions in helicopters and then the content delved specifically into rotor-rotor interactions in multicopters.

First and foremost, the interactions between the main rotor and the helicopter's fuselage have been thoroughly examined in the past through the utilization of validated numerical tools and experimental findings [5], [6]. Some of these tools included time-averaged and time-dependent fuselage pressure measurements, six-component balance measurements and particle image velocimetry (PIV) measurements. Especially, the PIV technique enabled the measurement of the instantaneous velocity field in large planes around the helicopter for several blade positions during rotor revolution. The impact of the rotor's downwash on the fuselage and its point of impingement are usually captured by test points at various advance ratios and rotor thrust coefficients [5]. Another interesting model that is able to express Fuselage-Rotor and Fuselage-Wake interferences uses a semi-empirical analytical formulation of the velocities that the fuselage induces. It provides the ability to analytically or numerically integrate the convection of the rotor wake, which allows for the calculation of the corresponding downstream displacement of rotor blade tip vortices within the given velocity field [6].

Additionally, there has been considerable research on the aerodynamic interactions between the helicopter and the ground [7], [8]. For instance, during an experiment of a model-scale tandem rotor system that used the PIV technique, velocities of the flow field were obtained in a vertical plane at four different aircraft azimuths. These measurements were taken for radial distances up to four times the rotor diameter [8]. It was found that the increase of the rotor height from the ground decreased the outwash velocity at all aircraft azimuths (Figure 8). However, at greater distances and increasing rotor height, the longitudinal axis had increasing outwash velocities, while the lateral axis had decreasing outwash velocities.

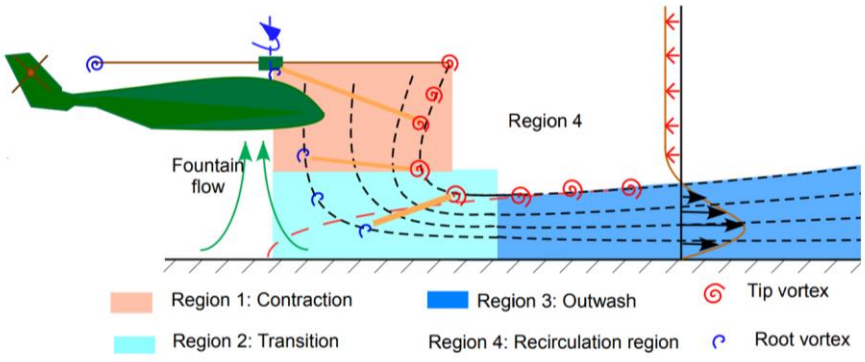

Figure 8: Regions of flow - Rotor in ground effect (M. Ramasamy et al., 2015).

Furthermore, the rotor-tail interactions are a crucial phenomenon for the reassurance of flight stability, thus it is probably one of the most documented topics in the helicopter industry. Noteworthy, the flight mechanics of a conventional helicopter can be significantly impacted by the aerodynamic interference between the main and tail rotor [9]. This interference may have a detrimental effect, resulting in notable unsteadiness in the loading of the tail rotor during specific flight conditions. However, the nature of this unsteadiness may vary based on the direction of rotation of the tail rotor. During intermediate-speed forward flight and right sideward flight of a counterclockwise main rotor, the entrainment of the tail rotor wake is delayed downstream by the free stream, resulting in minimal perturbations to the rotor loading. However, in left sideward and quartering flight, the entrainment process is confined close to the rotors by the free stream, leading to significant unsteadiness in the loads generated by the system.

Apart from aerodynamic interactions, crucial role plays the turbulence modelling on the accuracy of the study's results [10]. A recent paper tested various turbulence models such as SST k-ω linear eddy viscosity model, the BSL-RSM model and an Explicit Algebraic turbulence model with the aim of optimizing the nominal performance of a selected quadrotor propeller. It found that there were no significant differences between the pressure distribution and the aerodynamic interactions for each model. Nevertheless, the use of the BSL-RSM model appeared to be a sensible option for further analysis as it was capable of calculating the anisotropy of Reynolds stress and delivering more accurate forecasts for boundary layers that have undergone transition and detachment in intricate propeller flows.

Bearing in mind that Rotor-Rotor and Rotor-Propeller interactions were the main topic of this thesis and after the citation of introductory studies, the rest of the literature review was focused solely on interactional effects. These phenomena have been acutely under-researched creating a massive literature gap. Nevertheless, some of the few extensive researches that have been conducted were presented below.

An interesting study that followed the same validation steps as the DLR's Quadrotor was conducted at an octocopter in China. Computational analyses and verification experiments were both utilized in order to optimize the aerodynamic efficiency of the drone [11]. In order to address the limitations associated with conventional monolayer and coaxial octocopters, a new octocopter design was suggested. For a methodical and precise aerodynamic analysis, model analytics were carried out on five distinct octocopter drone models featuring three varied configurations, which comprised of a conventional configuration, a coaxial configuration, and a new configuration (Figure 9, Figure 10). In detail, CFD simulations were chosen to examine the effect of the rotors' blade size at the wind-rotor interferences and their impact on the efficiency and performance of the multirotor systems. At the end, the study presented a novel design for an octocopter drone utilizing a hybrid approach. The proposed configuration was found to produce 41.5% more thrust than a coaxially configured octocopter drone with identical rotor blade size and 71%

more thrust than a conventionally configured octocopter drone with the same fuselage arm length. Notably, this performance improvement was achieved without necessitating a more advanced flight control system.

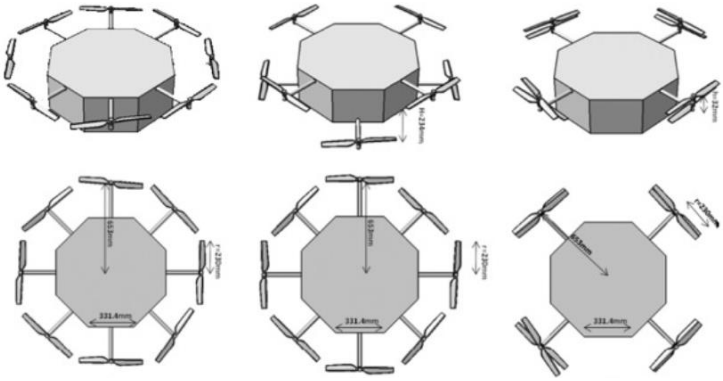

Figure 9: The three different configurations, (1) conventional configuration, (2) coaxial configuration, (3) new configuration (He Zhu et al., 2020).

Another investigation posed a valuable question regarding the comparison between the low Reynolds number of many UAV rotors (Figure 10) and the expected values obtained through conventional analytical methods for rotorcrafts. The study involved observing a pair of rotors positioned side-by-side during hover, while varying the rotor spacing and Reynolds number, utilizing high-speed Stereo Particle Image Velocimetry (SPIV) and other performance measurements. The SPIV data, both instantaneous and time-averaged, revealed that there was a rise in inter-rotor wake interactions as the rotor spacing and Reynolds number decrease. The study also highlighted a drop in rotors' efficiency at small rotor spacing and low Reynolds number through measurements of thrust and torque [12].

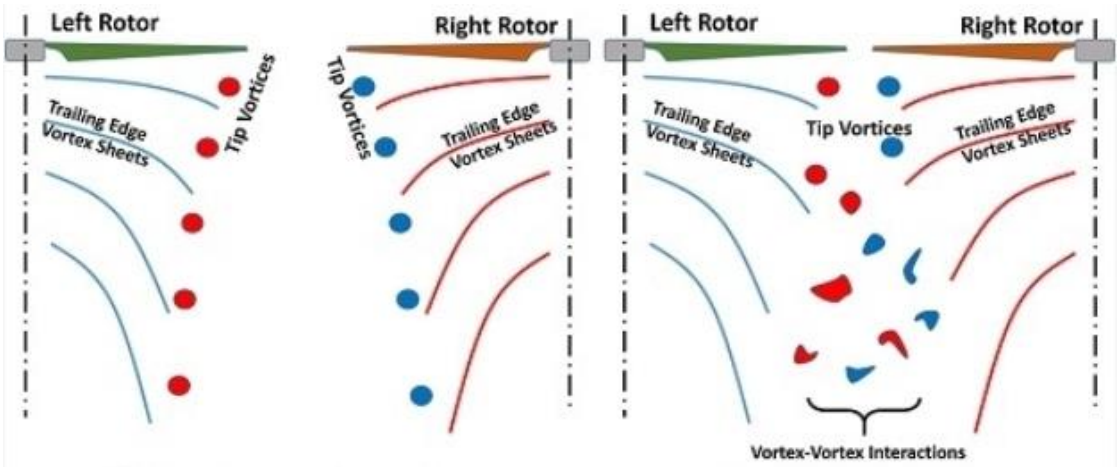

Figure 10: Non-interactive High Re wake & Interactive Low Re wake (D. Shukla et al., 2018).

In addition, the US Army created a project that had a scope similar to the one of this thesis. An evaluation was conducted to compare only the hovering capabilities of torque-balanced coaxial, tandem, and tilt-rotor systems against single-rotor systems with equivalent same solidity [13]. The variables of the experiment were the shaft-to-shaft distances for tandem rotors and the axial separation distance for coaxial rotors. Also, in terms of system performance both untwisted and highly-twisted blades were examined. The comparison of the configurations with a single-rotor determined several aerodynamic interferences and their corresponding loss factors, while nominal coefficients such as thrust sharing ratio, hovering efficiency of the rotor system, efficiency of the individual rotors, and the influence of one rotor on the other were also calculated.

Moreover, a study of a compound helicopter with side propellers that was conducted in 1967 had been the bedrock of this work [14]. Even though it is outdated, it was an extensive project that set the path for modern researchers. Unfortunately, during the tests a full aircraft was utilized which questions the results' fidelity due to the rife of extraneous interactions. In detail, the vibratory bending moments experienced by the wing-mounted tractor propellers were a direct function of the sum of the rotor momentum downwash angle and the geometric angle of attack. On the other hand, the vibratory bending moments of a tail-mounted pushed propeller were affected by the rotor lift, which depended on whether or not there was empennage forward of the propeller. Furthermore, the research revealed that increasing the thrust on wing-mounted tractor propellers typically led to greater rotor blade vibratory bending moments.

One of the most important and the most recent studies on interactional effects was conducted in 2016. The study focused on small scale rotor-propeller experiments aimed at defining the propulsive efficiency and relative vibration levels on tractor propellers that operate in the wake of a powered rotor and generic fuselage [15]. Six-component propeller loads were measured for all test points with a focus on thrust and torque. The propeller and main rotor were operated under conditions that imitate low- and high-speed vehicle flight, which replicated speeds ranging from 105 kts to 200 kts. The conclusions of this study were extremely useful since they clarified that the operation of the propeller did not have a discernible impact on rotor trim, but the performance of the propeller was significantly influenced by the main rotor states. When the propeller was operated in the rotor wake, all positions displayed a boost in propulsive efficiency compared to the isolated propeller data. Additionally, there were no noticeable differences in vibration levels between the different positions. Finally, the propulsive efficiency was highest for the propeller positioned at mid-height.

Last but not least, during the course of this thesis another paper that was associated with the DLR experiment was published. In that paper two-rotor systems were analyzed with the aim of bolstering the comprehension of interactional effects at simpler test cases prior to the study of the quadrotor. The two rotors were positioned in Side-by-side, Tandem and Oblique alignments. The Side-by-side rotors showed a 10% thrust gain and 20% torque

reduction compared to a single rotor test case which highlighted the configuration's positive effect [16]. On the other hand, the results were detrimental for the Tandem configuration since the second rotor was heavily affected by the downwash of the aft rotor causing an enormous decline in its produced thrust. Lastly, the Oblique configuration presented also encouraging results, since the first rotor's tip vortices, especially in high tilt angles, interacted positively with the second rotor and augmented its efficiency [16].

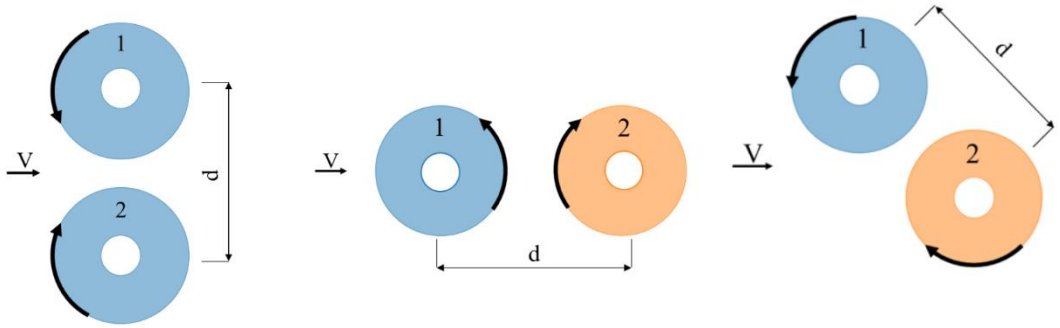

Figure 11: Side-by-side, Tandem & Oblique Configurations (Anna A. Kostek, 2023).

6. Methodology

The meticulous experiment that was conducted at the DRL was the stepping stone of this thesis since its collected data was utilized to validate the thesis' computational results. Therefore, this chapter detailed extensively the DLR's action research and recited the required steps to denature the experiment from physical to computational state. DLR explored the aerodynamics and aeroacoustics of small rotor blades and rotor-rotor interactions [3]. Nonetheless, only some of the experimental proceedings of the flow chart at Figure 12 were actually simulated through CORAL.

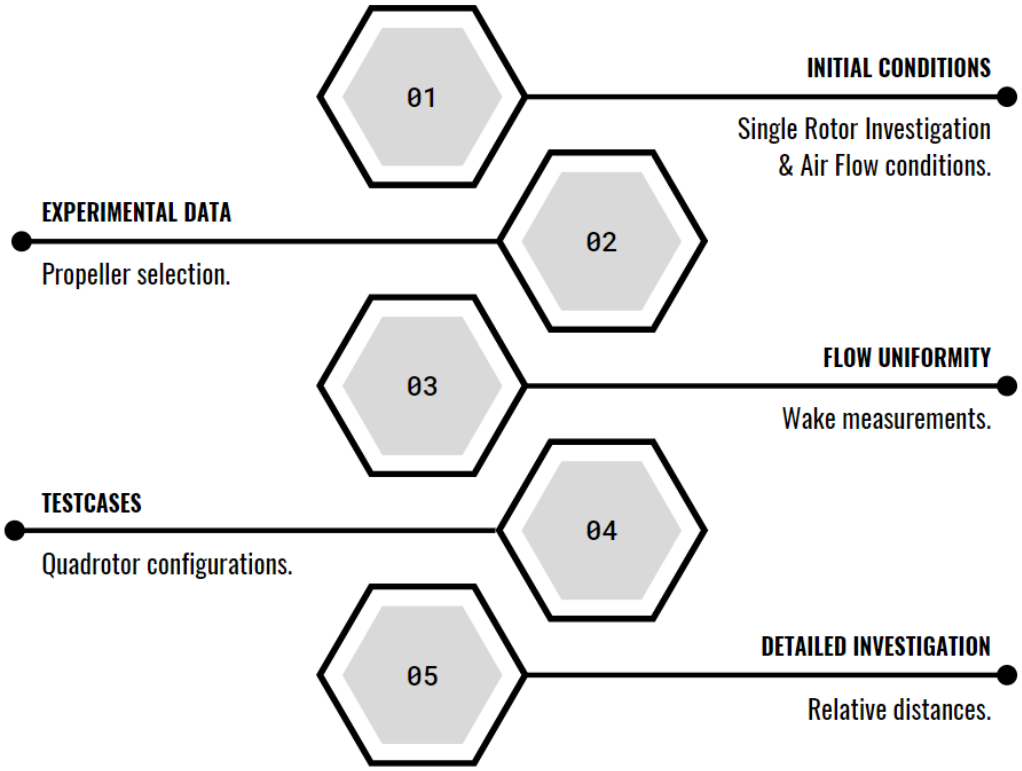

Figure 12: Flow chart of the DLR's experimental proceedings.

6.1.1 Experimental Set-up

Initially, the aerodynamics of a single rotor were studied which set the path for the first simulation. The physical rotor had a constant rotational velocity of 5400 RPM and the Eiffel-type wind tunnel nozzle of the test stand Göttingen (RTG) (Figure 13) exuded air with the velocity of 12.9m/s. To achieve these flow velocities a nozzle outlet of 1.6m x 0.8m was selected for the measurements. The same conditions were also set for the initialization of the CORAL's computations.

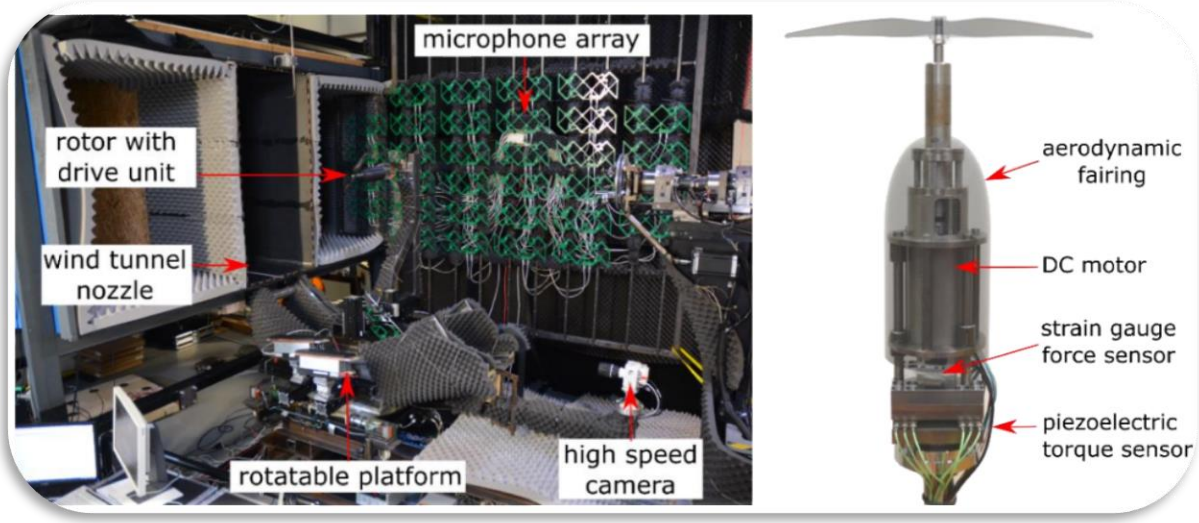

Figure 13: Experimental setup in RTG (R. Boisard et al., 2022).

Both two- and three-bladed rotors with diameters ranging from 30.5cm to 62.2cm were mounted vertically in the test section on a rotatable support system that allowed for rotor tilt angle variations between -30° and 30°. The four types of two-bladed propellers were KDE 12.5x4.3“, KDE 18.5x6.3", KDE 24.5x8.1" and Aeronaut CAM- Carb. Light 12x4.5“ (Figure 14), while the three types of three-bladed propellers were KDE 12.5x4.3", KDE 18.5x6.3" and KDE 24.5x8.1". The simulation took into account only the two-bladed KDE 12.5x4.3“ and the rest propellers are planned to be tested in the long run. Moreover, only the two tilt angles -10° and 10° as a whole rotor plane were computed.

Figure 14: Types of propellers - KDE 12.5x4.3“ & Aeronaut CAM- Carb. Light 12x4.5“ (A. Kostek, 2022).

6.1.2 Computational Methods - CORAL

The DLR realized the visualization of tip vortices in the rotor's wake by a background-oriented Schlieren (BOS) setup. Conversely, the wake simulation of the CORAL software is based on the use of the Helmholtz decomposition theorem, through which the influence of solid body components such as rotor blades or fuselage were captured along with the influence of their wakes (further information about the theorem are deposited below) [17]. Each body is described by a set of input files that determined its geometrical and kinetical characteristics and then it was divided by nodes into a number of sections which were defined perpendicular to the body reference line. The wing element between two consecutive sections formed a "strip". The strips were the main computational blocks for the local aerodynamic loads' calculation. As seen in Figure 15, these blocks varied depending on the selected CORAL's computational method. In L.L., each section had only two nodes describing the leading and trailing edge points of the airfoil, which therefore rendered its strips into flat plates. Additionally, the methods lifting surface (L.S.) and thick body (T.B.) were utilized. At L.S. each section was formed by more than two nodes, that actually followed the mean camber line of the airfoil. At the T.B. the nodes followed the exact airfoil's shape. Furthermore, the strips were divided into panels (Figure 15). Inside every panel, a single control point was defined, on which the local pressure (for T.B.) or the pressure jump (for L.S.) or yet the circulation (for L.L) was calculated.

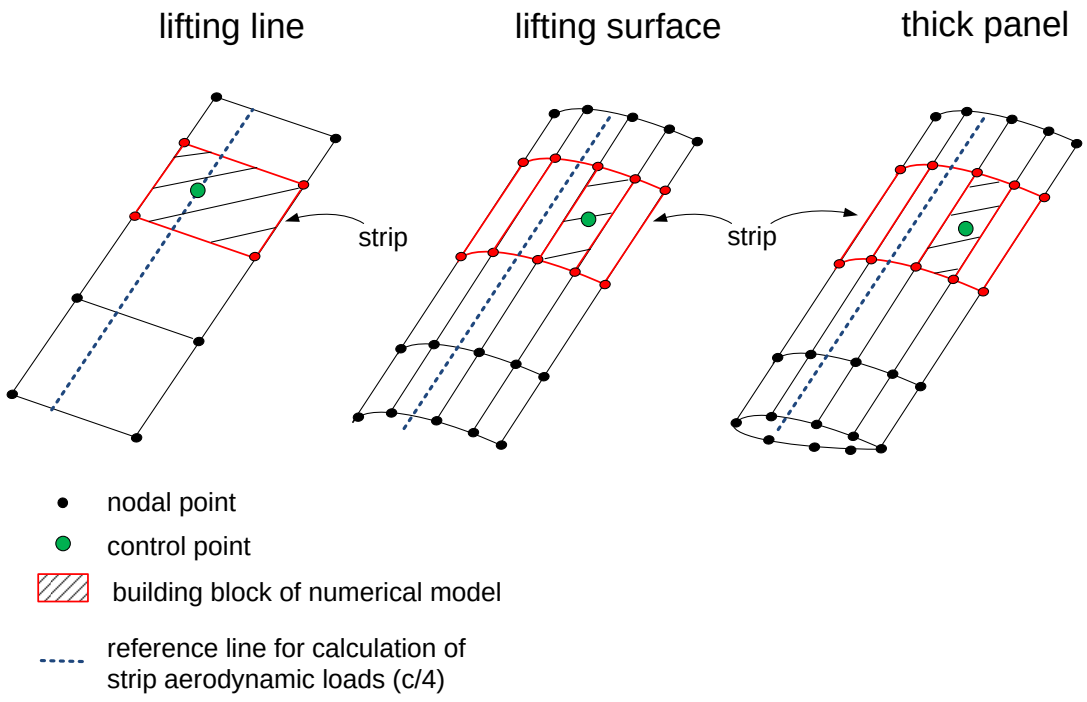

Figure 15: CORAL's computational blocks for the L.L, L.S., T.B. (V. Riziotis et al., 2019)

It is worth noting, that CORAL solved the incompressible and inviscid flow around the multi-component test cases and various viscous corrections were applied afterwards. All calculations were centered around the fact that the trailing edge nodes of lifting body sections released free wake lattice panels, which transformed into vortex particles (VPs), in a subsequent number of time steps, composing the far field (Figure 16). Basically, VPs were the combination of vorticities shaped by near-wake vortex lattice elements. That enabled VPs to move freely with the local flow velocity. Moreover, this combination saved enormous computational time, as it merged numerous wake panels in the spatial and temporal direction into sole VPs [18].

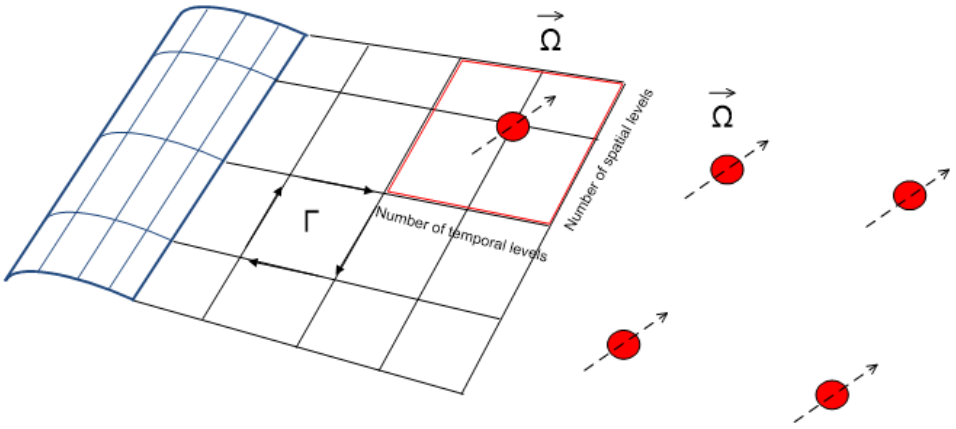

Figure 16: Conversion of the wake filaments into vortex particles (V. Riziotis et al., 2019).

6.1.2.1 Equations

According to the Helmholtz's theorem of vector calculus, the total instantaneous velocity of a control point situated at $\vec{x}_0$ at a determined time step is given by:

$$(1) \quad \vec{u}(\vec{x}_0; t) = \vec{u}_{ext}(\vec{x}_0; t) + \vec{u}_{solid}(\vec{x}_0; t) + \vec{u}_{wake}(\vec{x}_0; t)$$

In equation (1), the first component expresses the time-varying external field. The second component $\vec{u}_{solid}$ accounts for the $\nabla\Phi(x;t)$ of solid boundaries which usually is expressed, according to Green's theorem (2.a), by surface singularity distributions [17].

$$(2.a) \quad \Phi(x) = -\frac{1}{4\pi}\oiint\left[\frac{\vartheta\Phi}{\vartheta n}(s)\left(-\frac{1}{|x-S|}\right) - \Phi(s)\left(\frac{-(x-S)\cdot n(s)}{|x-S|^3}\right)\right]dS(s)$$

$\Phi(s)$ is the potential of the distribution of singularities on the surface S_D, x the position vector of the point where the potential is calculated, and the position vector of the singularity in the field. Additionally, the normal derivative of the potential at the point of the singularity, defined on the surface S_D may be calculated by the equation (2.b):

$$(2.b) \quad \frac{\vartheta \Phi}{\vartheta n}(s) = \nabla \Phi(s) \cdot n(s)$$

For the L.L., the contribution of bodies is considered by open "horseshoe" shape vortex filaments distributed over the strips. In the L.S. and T.B., the body contribution is considered by dipole and dipole plus source distributions, respectively, over the elements. The third velocity component includes the body wakes, which are composed by vortex filaments or VPs and it is expressed by Biot-Savart's law:

$$(3) \quad \vec{u}_{wake}(\vec{x}_0; t) = \int_{D_{\omega(t)}} \frac{\vec{\omega}(\vec{x}; t) \times (\vec{x}_0 - \vec{x})}{4\pi |\vec{x}_0 - \vec{x}|^3} dD$$

In (3), $D_{\omega(t)}$ is the whole computational domain. As seen, the individual particles vorticity vectors, $\vec{\omega}(\vec{x}; t)$, maintain a significant contribution to the local velocity, $\vec{u}_{wake}(\vec{x}_0; t)$. Interestingly, the wake deformation in time is calculated by the computation of local velocities at both the control points of the panels and every particle in the field [17]. To sum up, the overall potential of flow field disturbances consists of contributions from dipoles, sources, and vortices, since the solution is obtained through an indirect formulation. Nevertheless, the problem can be directly solved by replacing the normal derivative (velocity from the no-penetration condition) in the potential in order to perform a direct formulation. In L.L, as stated above, the bound circulation, $\vec{\Gamma}(\vec{x}_0; t)$, for every strip is computed by the solution of the discretized system of equations:

$$(4) \quad \vec{L}(\vec{x}_0; t) = \rho \vec{u}(\vec{x}_0; t) \times \vec{\Gamma}(\vec{x}_0; t)$$

The satisfaction of the nonlinear equation (4) occurs at each control point within the lifting line grid. Regarding the L.S and T.B., the kinematic boundary condition of non-penetration is fulfilled at the control points, specifically at the center point of each surface panel element. On top of that, the Kutta condition is met along the trailing edge (TE) line of all lifting bodies. In the latter two modeling options, there is no requirement to define the airfoil polar characteristics unless viscous corrections are applied. Remarkable is the fact that, when dealing with non-lifting bluff bodies, the procedure remains the same as for lifting thick bodies, except that the Kutta condition is not satisfied, and therefore, no wake emission occurs.

6.1.3 Noise Emissions

The rotor's noise emissions were measured using an innovative microphone array, consisting of 512 micro-electro-mechanical systems (MEMS) microphones. Coral was not able to compute whatsoever any noise emissions.

6.1.4 Configurations

Succeeding the single rotor investigation, the final testing included multicopter configurations with up to four rotors that could also be controlled in phase. These were the diamond, breaststroke and bearhug arrangements (Figure 18) [3]. The Figure 18 below depicted the direction of rotation for each propeller for every arrangement. The CORAL software simulated identically each and every one of these test cases.

The study also involved varying the relative distances between the rotors for the plus and cross configurations (Figure 20). These distances were presented as the symbol d in Figure 18. Last but not least, another parameter of the calculations was the tilt angle of the whole rotor plane. For the sake of this thesis, only -10° & +10° were studied.

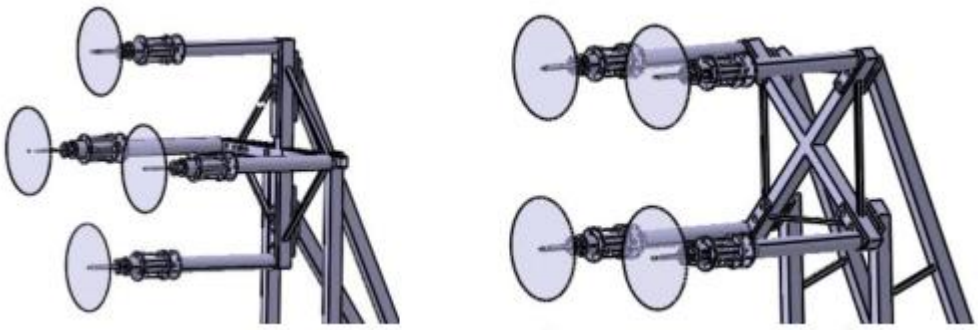

Figure 17: Plus and cross configurations (A. Kostek, 2022).

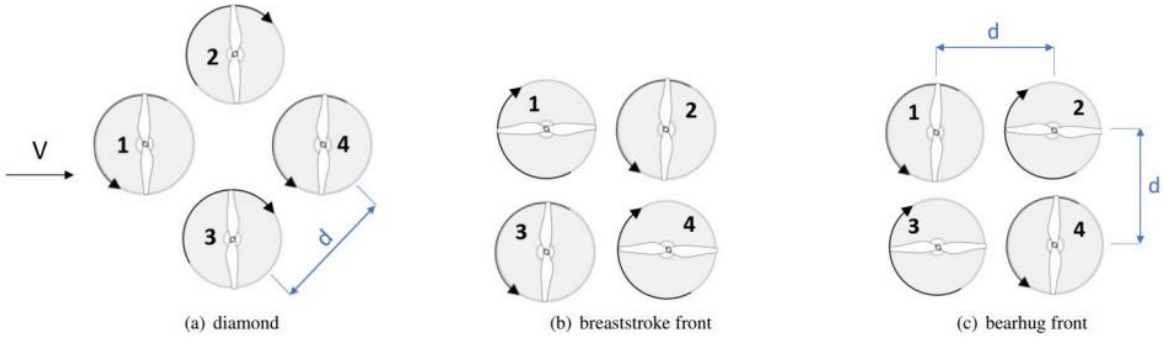

Figure 18: Test cases, relative distances and relative phasing of the propellers (R. Boisard et al. 2022).

(a) Tilt -10° (b) Tilt 10°

Figure 19: The two studied tilt angles -10° & +10° (Anna A. Kostek, 2023).

d Distance [mm]	533	457	381	335	305	266	230
d/D	0.72	0.84	0.96	1	1.22	1.44	1.7

Figure 20: Relative distances for the plus and cross configurations.

6.1.5 PIV Measurements

The DLR's activities also entailed the PIV measurement of the induced velocity distribution below the rotor. The reference plane was set 75mm away and parallel to the rotor as seen in the Figure 21.

Only the most interesting PIV test cases were calculated with CORAL and visualized through Tecplot. These test cases either presented enormous thrust reduction due to their configuration or generated high deviations between the computational results and the experimental data.

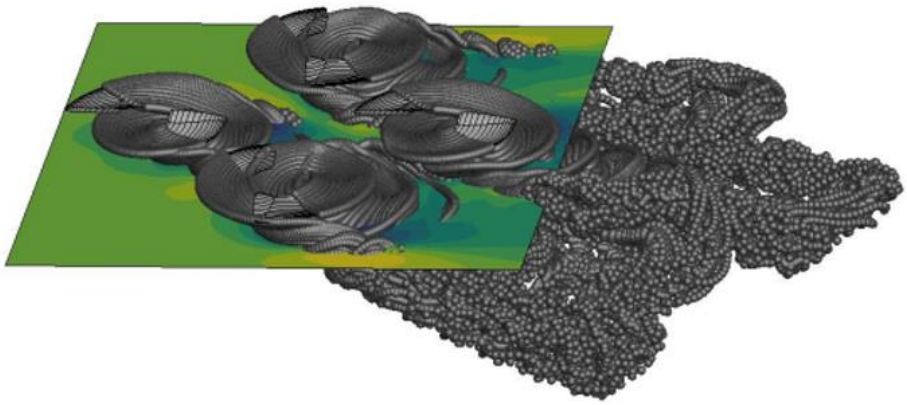

Figure 21: PIV measurements – Induced velocity distribution (A. Kostek, 2022).

7. Results

7.1 General Overview

In this chapter the computational results of the CORAL's Lifting Line (L.L.), Lifting Surface (L.S.) and Thick Body (T.B.) simulations were presented. These are the quadrotor's normalized mean Thrust and mean Torque for every configuration. From now on the normalized mean Thrust and Torque will be addressed simply as Thrust and Torque. The normalization was made by the Thrust and the Torque of a single rotor case which was also simulated. The single rotor normalization was a helpful tool that contributed to the rapid comparison of the flow advancement in the case of four rotors instead of a single one. Therefore, the results served a twofold aim. On the one hand, they validated the CORAL's accuracy in comparison with the experiment. On the other hand, they displayed the percentage of deviation from the single rotor test case. It is also worth noting that every simulation took into account potential flow conditions and then corrected them to viscous ones. Thus, in order to highlight the effectiveness of these corrections both the potential and the viscous results were depicted at the corresponding figures below. Chronologically, bearhug was the first configuration that was simulated. Next was the breaststroke and last the diamond since it was the most complex test case. The results were plotted with the use of Matlab. As seen below the Y axis labels presented the various thrusts and torques, while the X axis labels presented the various distances d between the rotors normalized by the propeller's diameter D=31.22cm (12.29 inches) (Figure 18).

7.2 Experimental Data

Generally, the experimental data showed that in the bearhug and the breaststroke test case the thrust of the front rotors was increased, whilst the thrusts of the aft rotors was decreased both for positive and negative plane tilt. Regarding to the torque of these test cases it seemed that it remained intact, something that contradicted the computational results. For the diamond test case the thrust and the torque of the first three rotors was augmented due to the configuration, independently of the distancing, while the last one was dipped into the wake of all the others and experienced detrimental results.

Moreover, it is vital to highlight the fact that considerable deviations were noted among the experimental data and the computed torque values at the front rotors of the square test cases for a positive plane tilt. The CORAL overestimated apparently the amelioration of efficiency for those cases. It is possible that the overrated computational results failed to take into account any local stall conditions that may have occurred on the experimental aft blades.

7.3 Computational Results

As stated above, the experiment was simulated through the lifting line (L.L.), the lifting surface (L.S.) and the thick Body (T.B.) methods. The computational results demonstrated good agreement with the measured data for all test cases at a negative rotor plane tilt. For a positive rotor plane tilt, the trends were also accurate, but there was a noticeable deviation in the magnitude of numerical torque estimations (Figure 23,Figure 24,Figure 25,Figure 26,Figure 27). Specifically, each and every one of the configurations, the bearhug, the breaststroke & the diamond, diverged significantly in the case of a plane tilt +10° and potential flow conditions. Lastly, for the diamond test case, the differences were examined individually at each rotor and not in pairs since there was no symmetry among them.

7.3.1 Square Configurations

The results indicated that the interactions observed in the square alignments had detrimental effects for all the analyzed rotor spacings. However, a slight overlapping of blades proved to be more beneficial than wider or nearer hub separations. Particularly, the highest overlapping rotor positioning resulted in a decrease in thrust and a notable reduction of torque. Notably, the interactional effects on torque were insignificant for larger hub spacings and negative plane tilt.

7.3.1.1 Front rotors

The square positioning, bearhug and breaststroke, influenced the front rotor performance positively. However, crucial effects were observed when the front rotors were very close to each other in Side-by-Side formation, around d/D=1. In such cases, there was an increase in thrust of up to 10% and a reduction in torque, by 5% for negative and up to 25% for a positive plane angle, compared to a situation where the rotor was isolated. These effects occurred due to the creation of an upwash region between the rotors caused by their united tip vortices. Nevertheless, for even closer rotor positions and a positive tilt angle, the differences between the experimental results of bearhug and breaststroke configurations became evident. The breaststroke configuration was characterized by stronger advancing side vortices that lowered the demanded torque, hence was found to be more favorable. Yet, that was not calculated by the CORAL.

7.3.1.2 Aft rotors

The aft rotors experienced a significant efficiency decline due to their operation within the preceding rotors' downwash and particularly their wake from the advancing side. The interactional effects exacerbated as the distance between the rotors decreased leading almost up to a 20% thrust reduction and a 5% torque increase for the negative and up to 40% for the positive plane angle.

7.3.1.3 Total Performance

As a whole, the observed phenomena were partly attributed to changes in the wake geometry of the front rotors caused by their mutual interaction.

As the separation between rotor 1 and 3 decreased, their tip vortices began to connect, forming a super-vortex and creating a strong local upwash region. This connected vortex propagated upwards, while its ascending tendency was more apparent in the bearhug configuration due to the interaction of the two retreating side tip vortices. However, the system's aggregated performance was actually negatively affected by the front rotors' wake, resulting in a reduction of the thrust produced at rotors for the negative tilt angle and the positive tilt angle. Furthermore, the performance of both square systems significantly declined as the rotor spacings increased. The cause of these effects was primarily the interaction of the aft rotors with the outer tip vortices of the preceding rotors. What is more, that decline continued to occur also for even larger hub distances, but the rotors were affected by the downwash of an inner wake this time which was also initiated by the preceding rotors (rotors 1 and 3). As a result, the thrust produced by the rear rotors fell by 30% for the nearest distance of d/D=0.74. However, in the breaststroke configuration, the retreating side vortices from rotors 1 and 3 were able to reach the level of rotors 2 and 4 creating an upwash region at distances with d/D<1. In those regions, the thrust produced by rotors 1 and 3 increased as the hub spacing started to decrease, reaching +10% for a -10° tilt angle and +15% for a +10° tilt angle.

To summarize, for both square configurations, the results indicated similar trends for the front and the aft rotors, demonstrating that both the improvement of the front and the deterioration of the aft rotors were triggered by the interactional effects related to their hub distance.

7.3.2 Diamond Configuration

The performance of rotors 2 & 3 was enhanced due to the influence of the tip vortices from rotor 1, both from its retreating and its advancing side as the spacing widened. Actually, all the beneficial effects were prodigious for the wider rotor spacings. It is important to note that in the diamond configuration, the distance between the side rotors and rotor 1 in the flight direction was actually shorter than the defined hub distance and was equal to $d/\sqrt{2}$. Moreover, for rotor spacings closer than d/D=1.44, the side rotors operated partially behind rotor 1 in parallel with the flow. As a result, for the closest hub spacing, rotors 2 and 3 suffered conditions comparable to those of the tandem aft rotors in the square configurations. In that case, as mentioned previously, the interactional effects became detrimental to the efficiency of rotors 2 and 3. Lastly, the influence of the middle rotors on rotor 4 was more significant than its interaction with the first rotor.

In addition, the degrading interactional effects on rotor 4 regressed, although not to the same detrimental extent of the aft rotors in square configurations, for the non-overlapping positions. The same went for the overlapping positions, where the performance of rotor 4 deteriorated rapidly and its thrust loss exceeded the corresponding calculations at rotors 2 and 4 in the square system reaching almost 40%. On the other hand, the efficiency of rotor 1 increased for the same overlapping conditions due to its tip vortices, reaching an improvement of up to 8% for a negative plane tilt and up to 10% for a positive plane tilt.

Additionally, the improved performance of the middle rotors 2 & 3 for the non-overlapping distances in the diamond test case began to deteriorate when the rotor positions became closer than d/D=1, as the rotors 2 & 3 started operating partially within the downwash generated by the inner wake of the front rotors.

7.4 Experimental Data & Computational Results

The overview of CORAL's data accuracy was exceptional. Very few results diverged significantly from the experimental data, while in most cases they coincided. Nonetheless, as stated above there were a few cases where the magnitude of CORAL's results exceeded the experimental data.

7.4.1 Bearhug

For the bearhug test case with a plane tilt +10° and potential flow conditions (Figure 23) the L.S. results were superior against the other methods. The maximum torque differences for the front rotors were:

- 62% - L.L.
- 42% - T.B.,

while the L.S. dropped significantly at:

- 23% - L.S.

However, at the aft rotors the most inferior method was T.B. since there the maximum torque differences were built up to:

- 40% - L.L.
- 68% - T.B.

For viscous flow all methods diverged at most 25% from the experimental data.

7.4.2 Breaststroke

For the breaststroke test case with a plane tilt +10°and potential flow conditions (Figure 25) L.S. results were superior against the other methods. The maximum torque differences for the front rotors were:

- 55% - L.L.
- 30% - T.B.

while the L.S. dropped significantly at 5%. However, at the aft rotors the most inferior methods were T.B. & L.L since there the maximum torque differences reached:

- 35% - L.L.
- 34% - T.B.

For the viscous flow all methods diverged at most 25% from the experimental data.

7.4.3 Diamond

At the diamond test case with a plane tilt +10°and potential flow conditions (Figure 25), L.S. results proved to be again superior against the other methods. The maximum torque differences were:

- 1st rotor: 54% - L.L and 30% - T.B., while the L.S. dropped significantly at 10%.
- 2nd rotor: 76% - L.L and 50% - T.B., while the L.S. dropped significantly at 11%.
- 3rd rotor: 51% - L.L and 30% - T.B., while the L.S. dropped significantly at 24%.
- 4th rotor: 45% - L.L and 70% - T.B., while the L.S. dropped significantly at 10%.

For the viscous flow all methods diverged at most 30% from the experimental data.

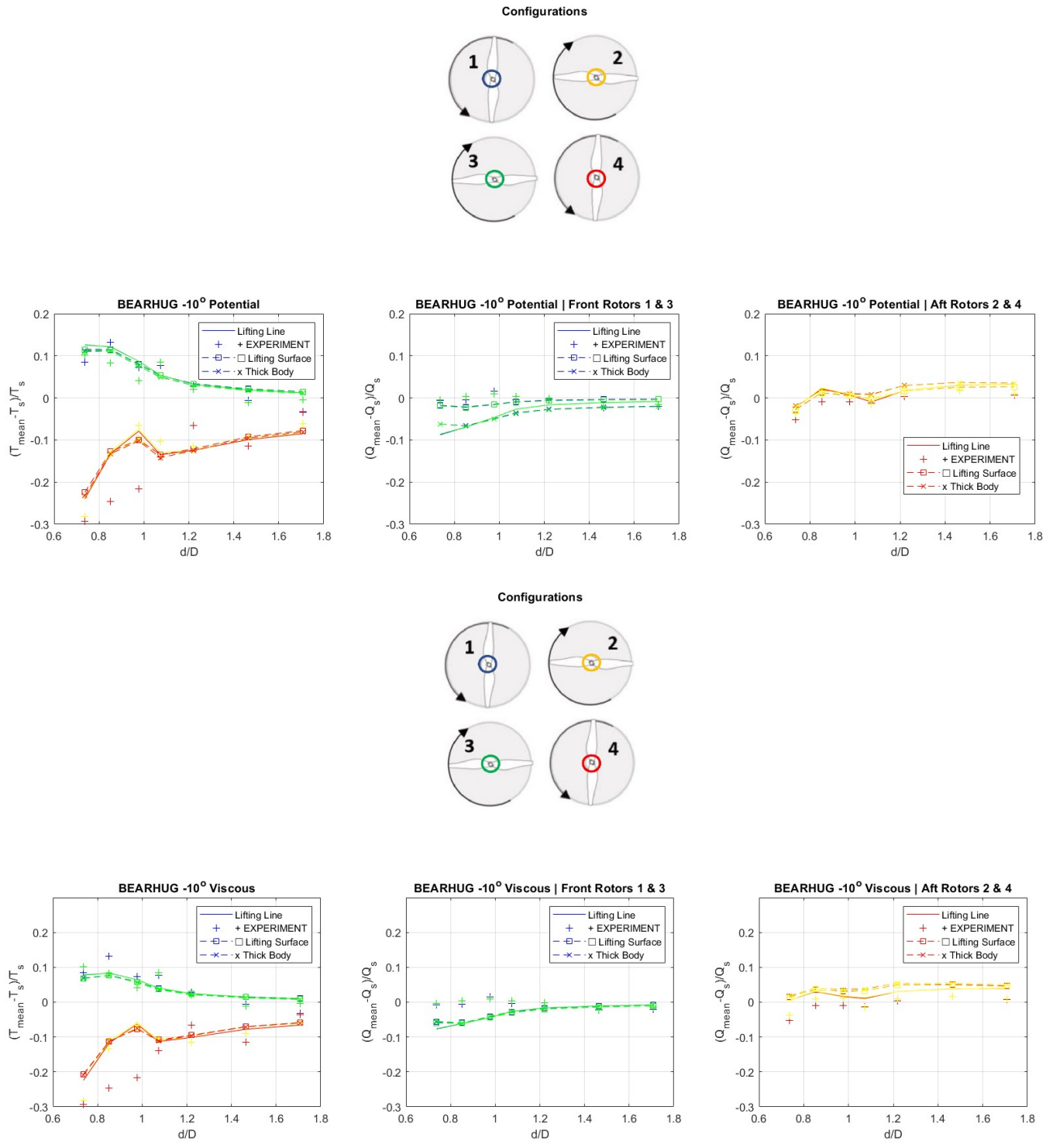

Figure 22: Bearhug Configuration – Plane tilt -10° – Potential & Viscous.

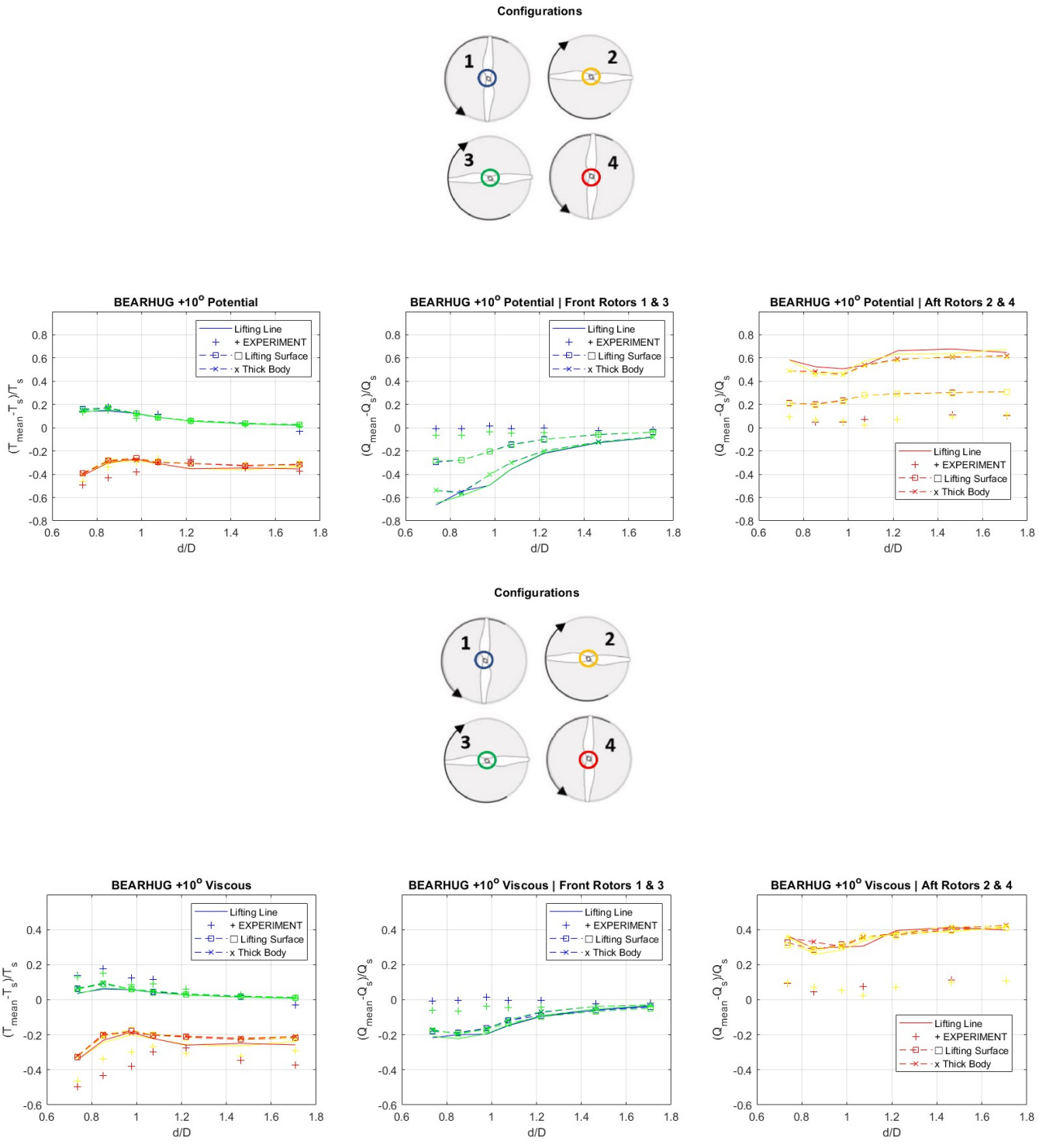

Figure 23: Bearhug Configuration – Plane tilt +10° – Potential & Viscous.

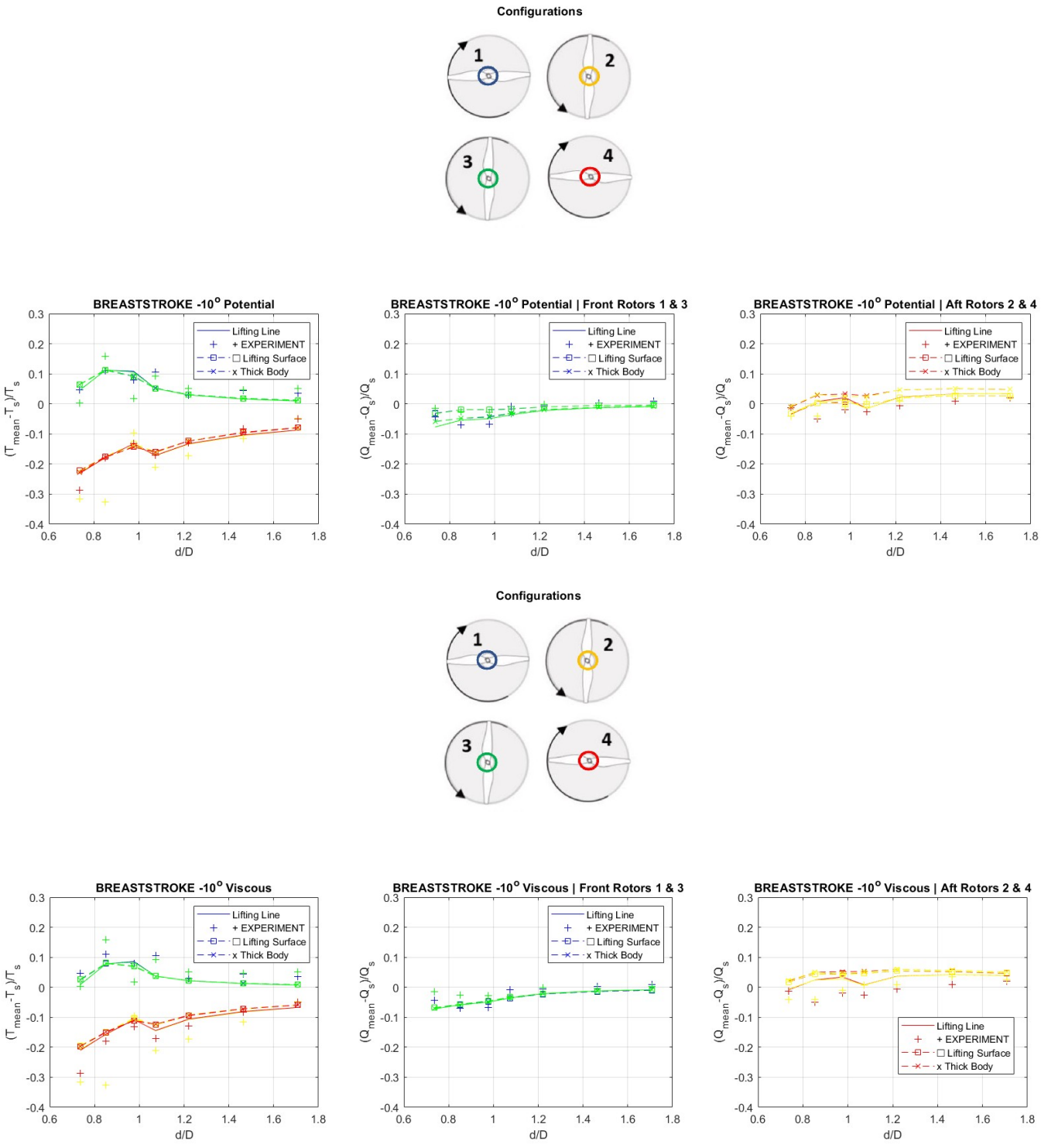

Figure 24: Breaststroke Configuration – Plane tilt -10° – Potential & Viscous.

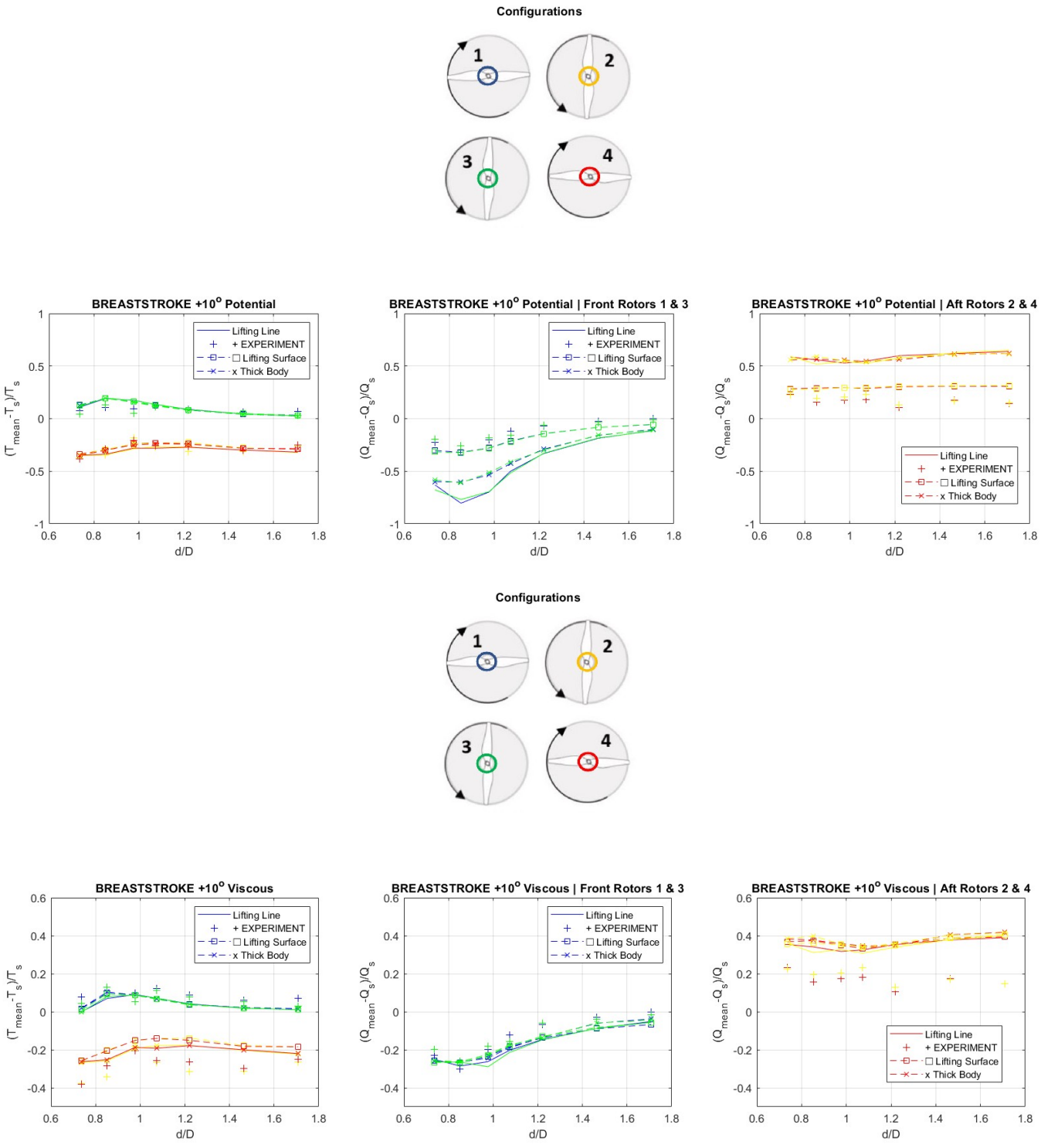

Figure 25: Breaststroke Configuration – Plane tilt +10° – Potential & Viscous.

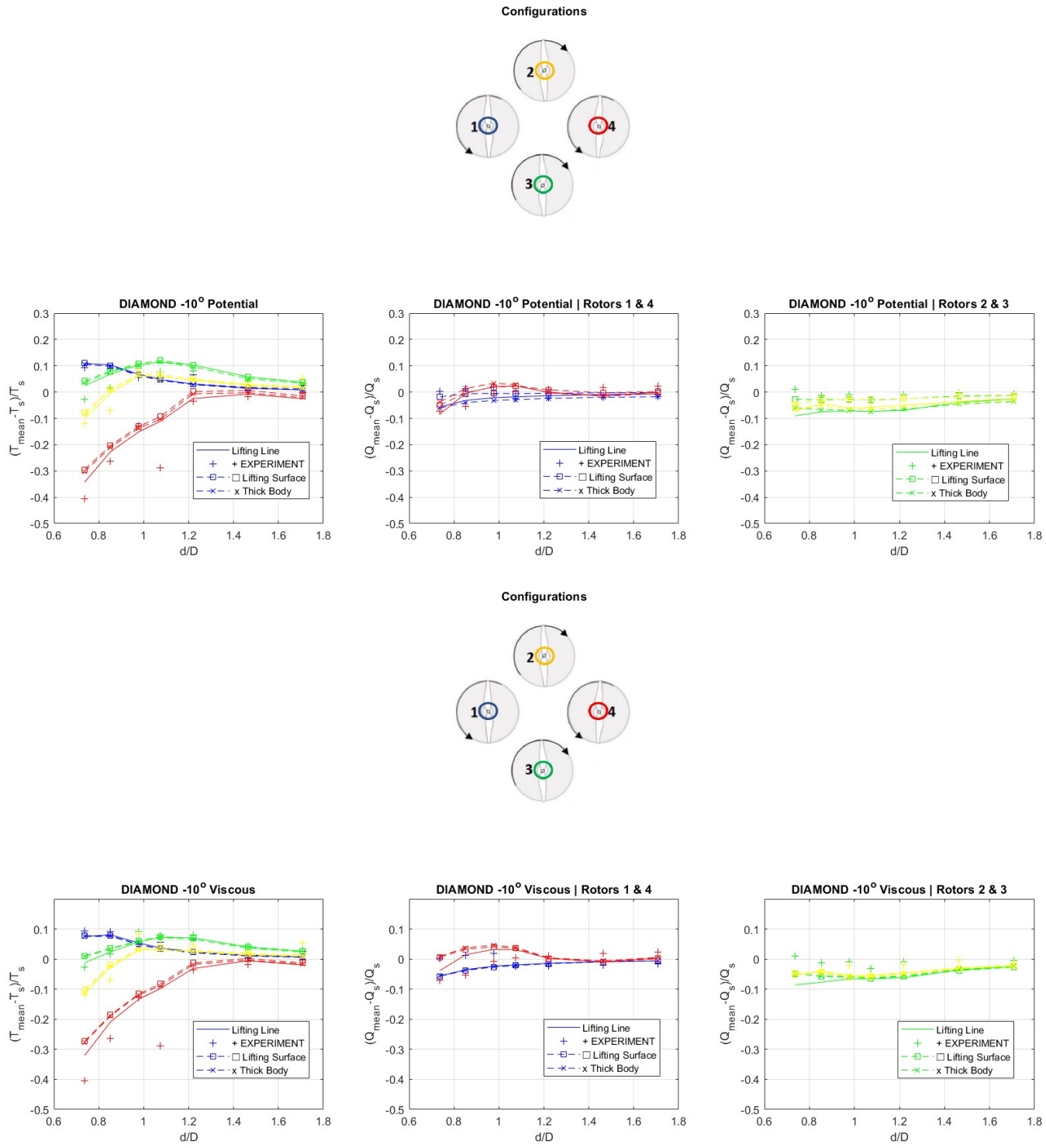

Figure 26: Diamond Configuration – Plane tilt -10° – Potential & Viscous.

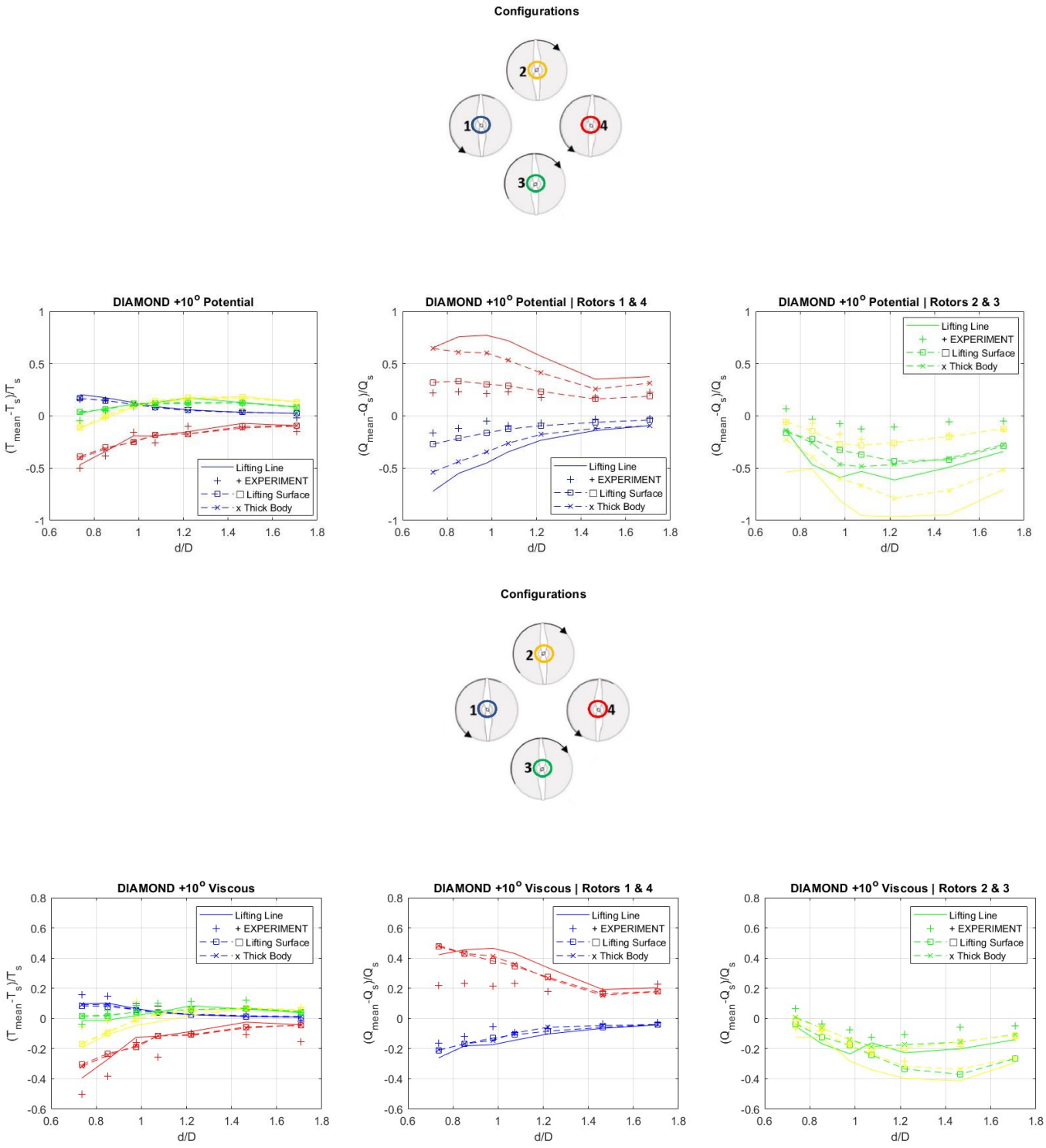

Figure 27: Diamond Configuration – Plane tilt +10° – Potential & Viscous.

7.5 Overall Efficiency & Power

The preceding analysis focused specifically on the local interactions of each test case. Also, in the previous chapter the superiority of the diamond test case among the others had prevailed. However, that local superiority was not inextricably intertwined with an actual totally enhanced efficiency against the single rotor test case. Therefore, in the Figure 28 every system's aggregated thrust and torque were proportionally compared to the ones that four isolated single rotors would generate in order to shape an all-round final opinion. In these graphs, a mean thrust higher that one represents a system that outperforms the four single rotors, also a mean torque less than one represents a system that requires less power to operate than the four single rotors.

As stated above, both square test cases, bearhug and breaststroke, revealed that the alignment of the front rotors in a Side-by-Side configuration was extremely beneficial for their thrust. However, the operation of the aft rotors within the downwash of the front rotors had a detrimental impact on thrust and torque, exceptionally for the non-overlapping and the intense overlapping cases, as seen at first and the last points of the corresponding thrust graphs. The approximate thrust reduction in Figure 28 reached 15%, while the simultaneous increase of torque ramped over 18%. Thus, the most efficient hub distancing d/D for both square configurations and a negative plane tilt was 0.96, which accounted for a slight blade overlapping. In addition, for the negative plane tilt a 5% decrease of thrust was observed for the spacing d/D=1.68 at both the bearhug and the breaststroke configurations. Yet it was onerous to discriminate which system required less torque as the distances converged. If that was not the case, one would be rendered as more efficient. Nevertheless, for a positive plane tilt both square systems exhibited a notable decrease in performance as the rotor spacings widened, that resulted in a 10% reduction in thrust and a simultaneous increase in torque by approximately 20%. It is intriguing to underscore that the bearhug and breaststroke configurations demonstrated optimal performance for the positive plane tilt at the overlapping distance of d/D=0.84. At variance with the previous ambiguous situation, the positive plane tilt presented lucidly that the breaststroke configuration outperformed the bearhug system in terms of efficiency.

Complementary, a closer look at Figure 28 validates the superiority of the diamond test case. First and foremost, for both the negative and the positive plane tilt and non-overlapping blades (d/D > 1), the thrust augmented over 1%. For the negative rotor plane tilt especially, the maximum proportional enhancement of thrust reached 2.5% for d/D=1.2. Additionally, for the negative plane tilt the torque plunged at around 2.5%, regardless of the blades distance. These data were tenable grounds that verified the diamond's test case favorability over the others.

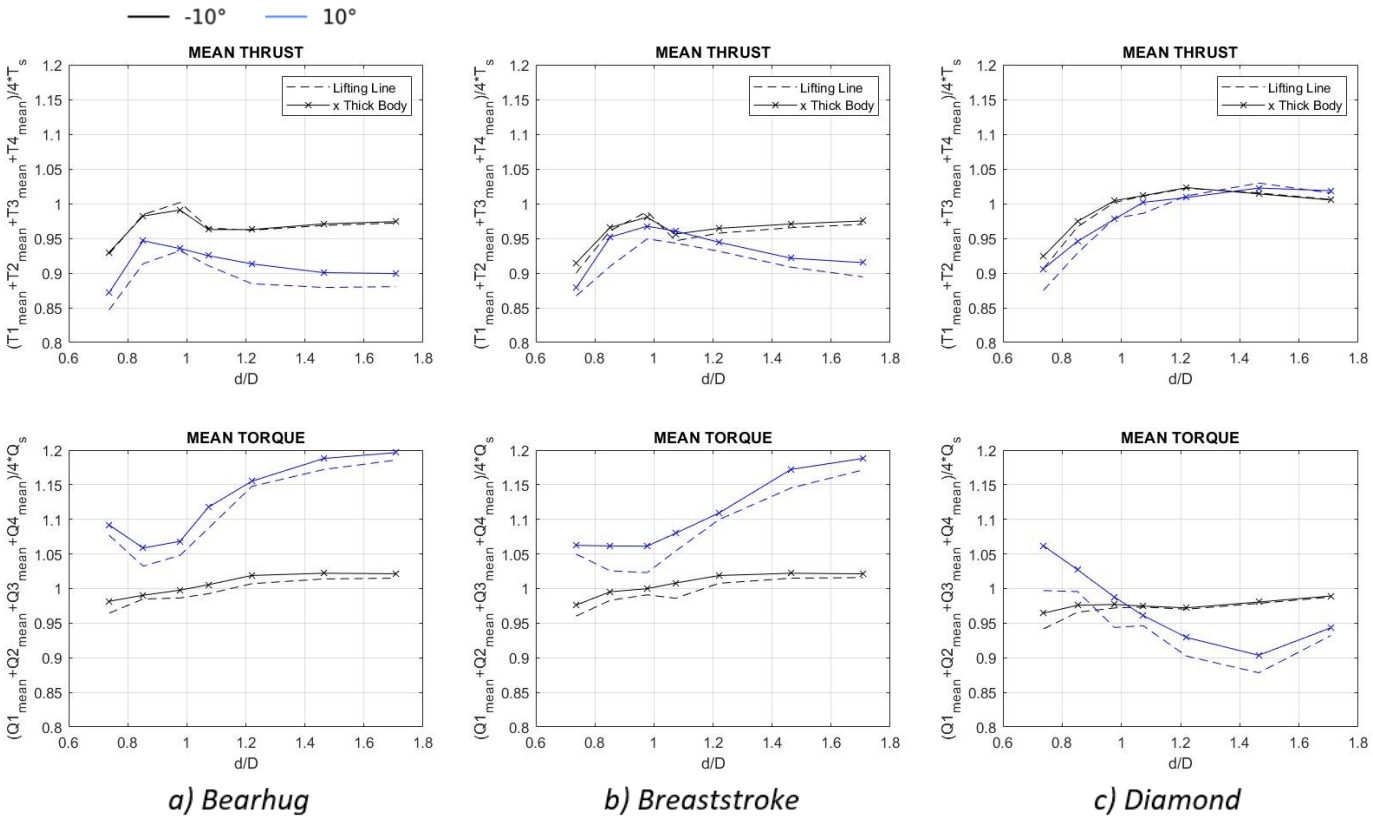

Figure 28: Change in the system's overall mean Thrust & Torque for every test case.

7.6 PIV Measurements

The extreme deviations of the torques at the positive plane tilt generated the necessity for further research. Therefore, another method was also utilized in order to interpret the data. That method was the PIV simulation and it was used as a subsequent validation tool that shed light upon the questionable square test cases. Among these cases were hub distances that either presented enormous thrust reductions due to their configuration or generated high deviations between the computational results and the experimental data. For the sake of this thesis, only the bearhug test case was simulated through the PIV method, as the velocity fields were pretty similar with the breaststroke. The results were plotted with the use of tecplot360.

7.6.1 Front rotors – Bearhug

The square positioning influenced the front rotors' performance positively. The most notable effects were observed when the front rotors were very close to each other in Side-by-Side formation. The front rotor's tip vortices shaped an upwash region between the rotors. As the separation among them decreased, their tip vortices began to connect, forming a super-vortex and creating a strong upwash region represented with orange color

in Figure 29. This connected vortex propagated upwards, and its ascending tendency was more apparent in the bearhug configuration due to the interaction of two retreating side tip vortices.

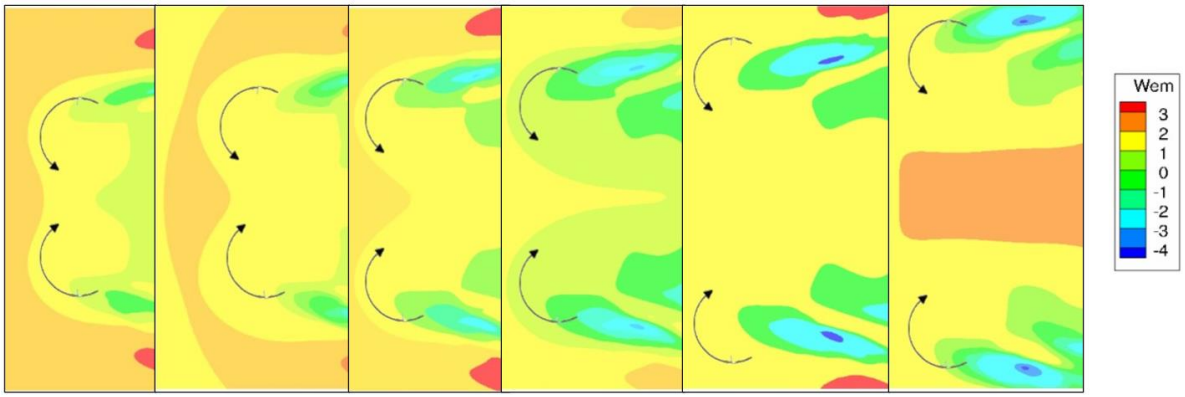

Figure 29: PIV - Velocity field of the front rotors for increasing hub distances.

7.6.2 Aft rotors - Bearhug

The most convoluted cases for the aft rotors were the ones with no overlapping or extremely intense overlapping. As the rotor spacings increased and the downwash regions widened, the interaction of the aft rotors with the advancing side's outer tip vortices, that had formed the preceding rotors, caused a significant performance decline. That decline continued to occur also for even larger hub distances, but the rotors were affected by the downwash of an inner wake this time which was also initiated by the preceding rotors as seen in Figure 30. Conversely, for the most extreme distances the aft rotors did not interact one with the other, thus a strong upwash layer was formed among them.

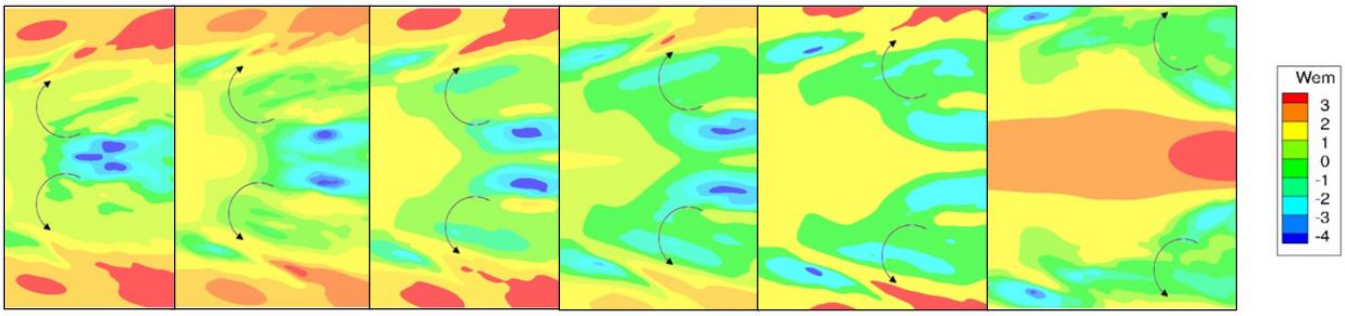

Figure 30: PIV – Velocity field of the downwash region among the front rotors for intense overlapping, slight overlapping & no overlapping.

7.6.3 General Overview - Bearhug

The figures below depict the velocity fields of the bearhug test case at the positive tilt angle for all the various hub distances d/D. The red, yellow and green regions presented the generated upwash, while the pale green and the blue regions the downwash. As seen in all figures, an intense downwash was evident right after the advancing sides of the aft rotors, yet the same occurred at the advancing sides of the front rotors as the hub distances started to increase. As cited above, the optimal performance for both square configurations at the positive plane tilt was achieved at a rotor spacing with slight overlapping blades at the distance d/D=0.84. Its corresponding velocity field has been depicted in Figure 33.

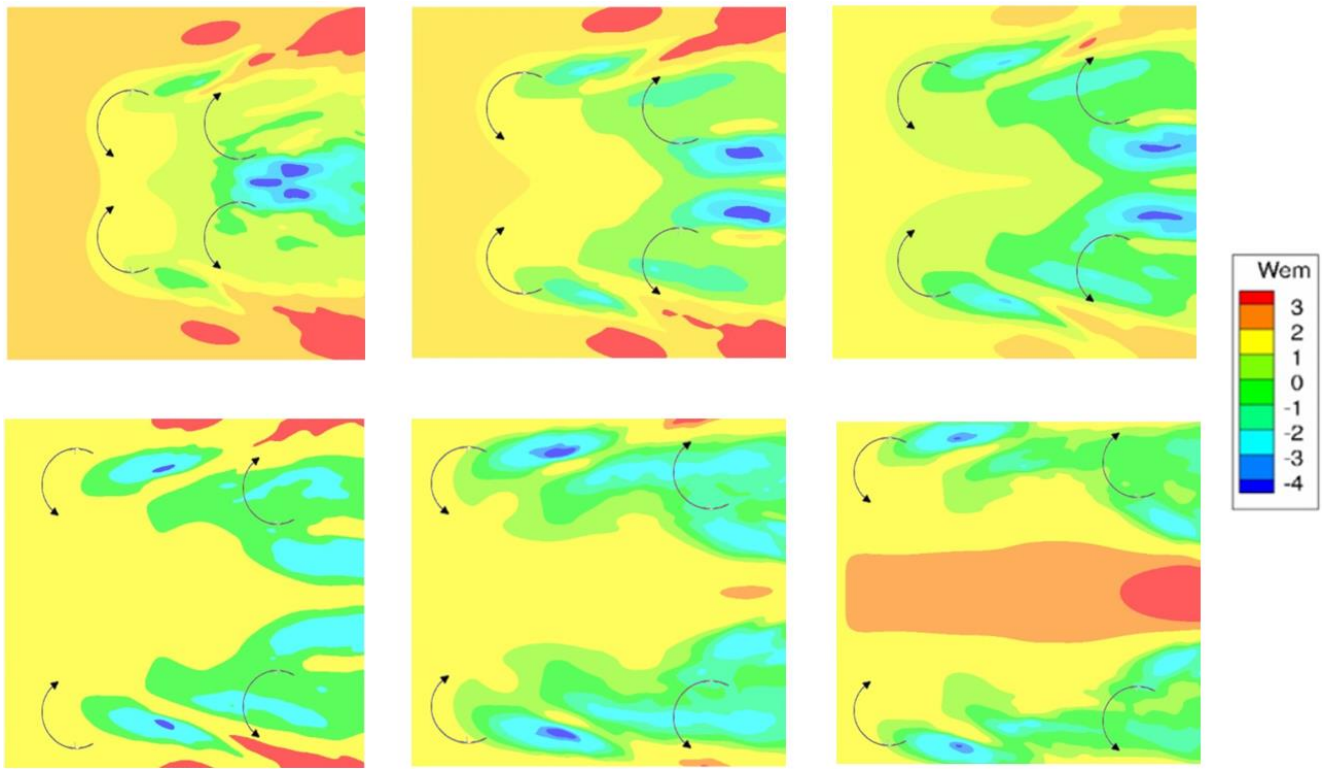

Figure 31: PIV - Velocity field of the quadrotor for increasing d/D.

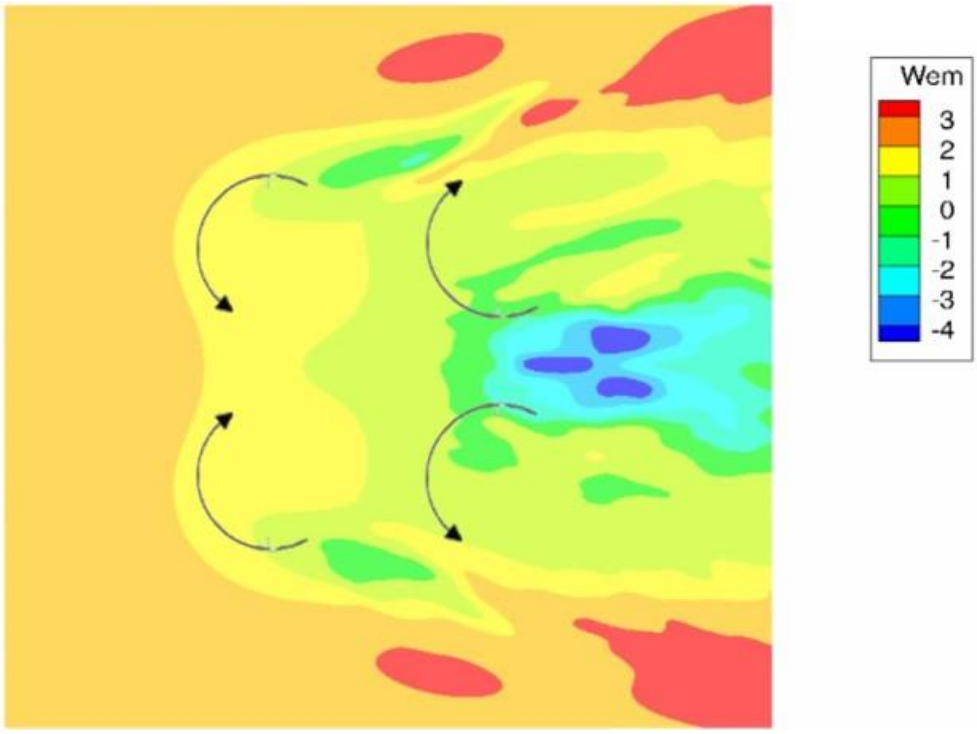

Figure 32: PIV - Velocity field of the quadrotor for d/D=0.74.

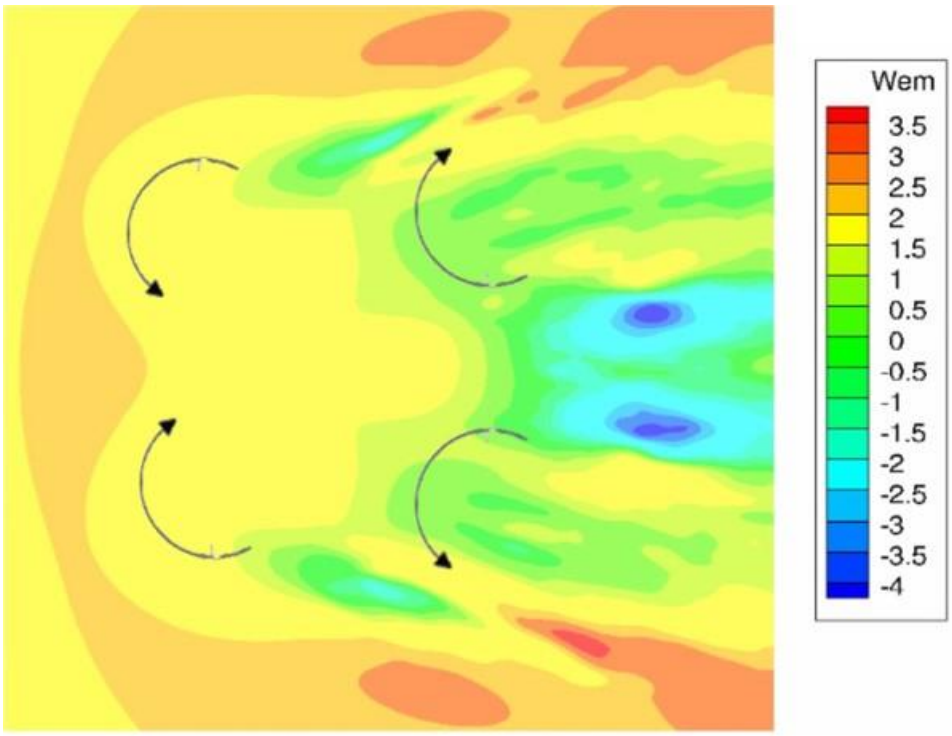

Figure 33: PIV - Velocity field of the quadrotor for d/D=0.84.

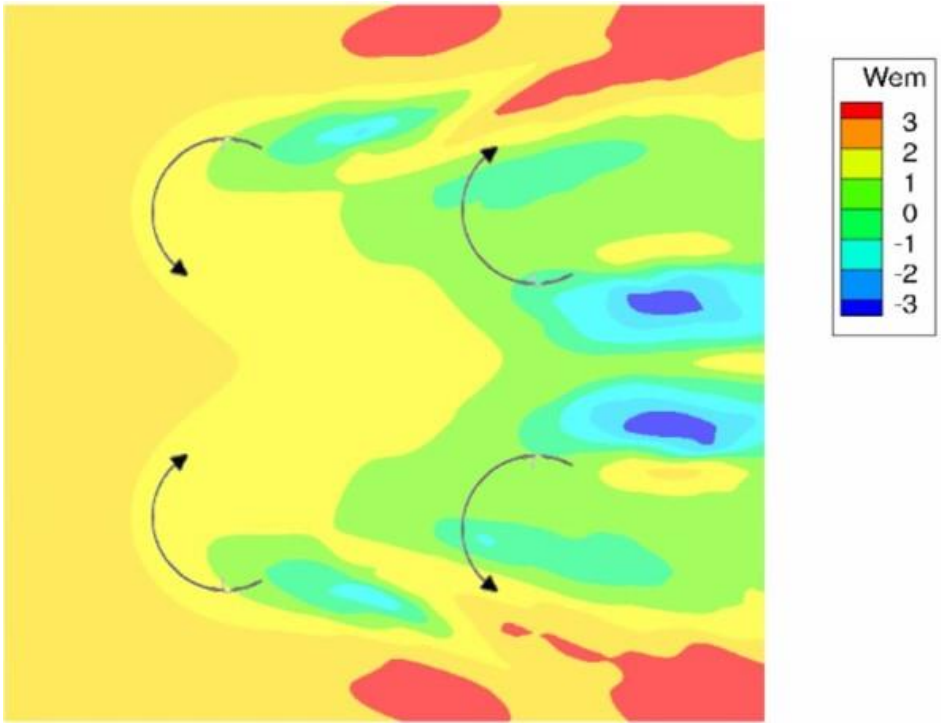

Figure 34: PIV - Velocity field of the quadrotor for d/D=0.96.

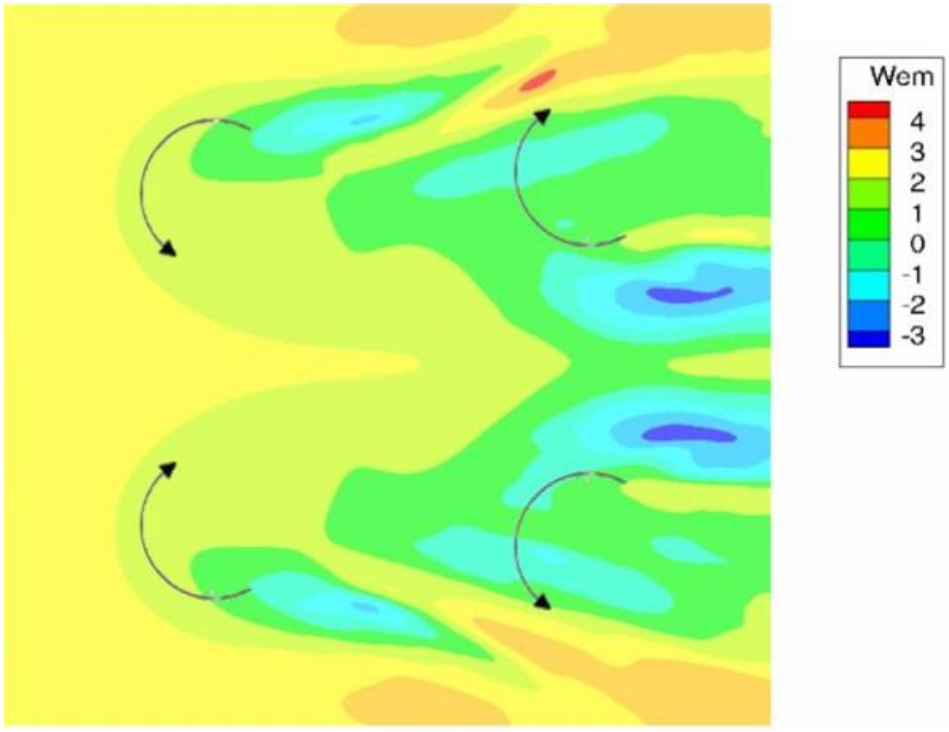

Figure 35: PIV - Velocity field of the quadrotor for d/D=1.

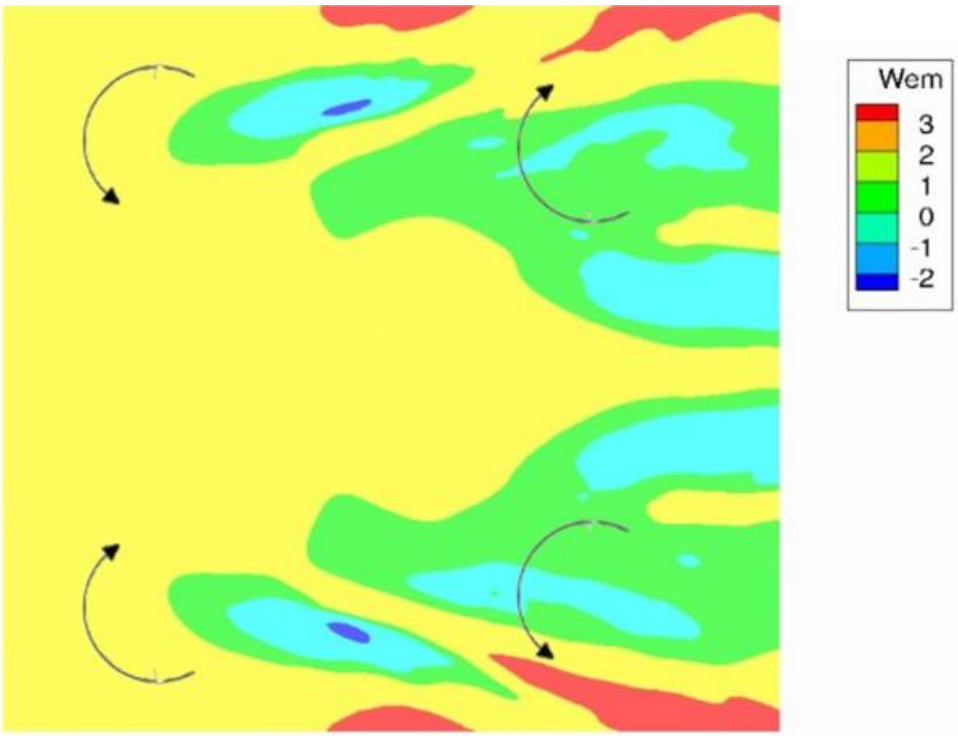

Figure 36: PIV - Velocity field of the quadrotor for d/D=1.22.

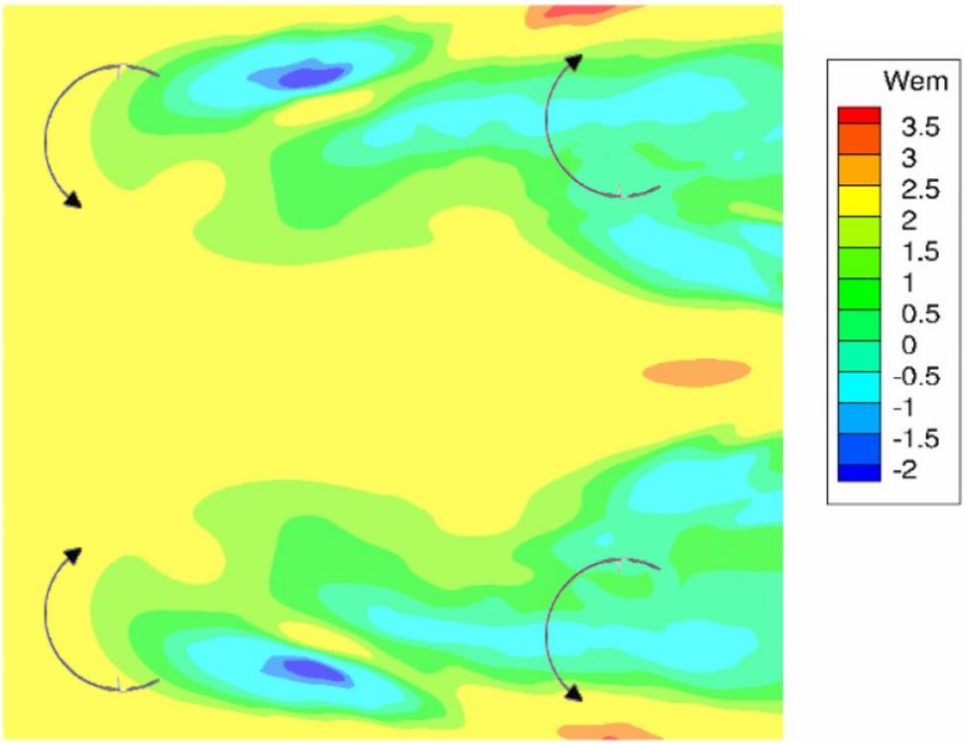

Figure 37: PIV - Velocity field of the quadrotor for d/D=1.44.

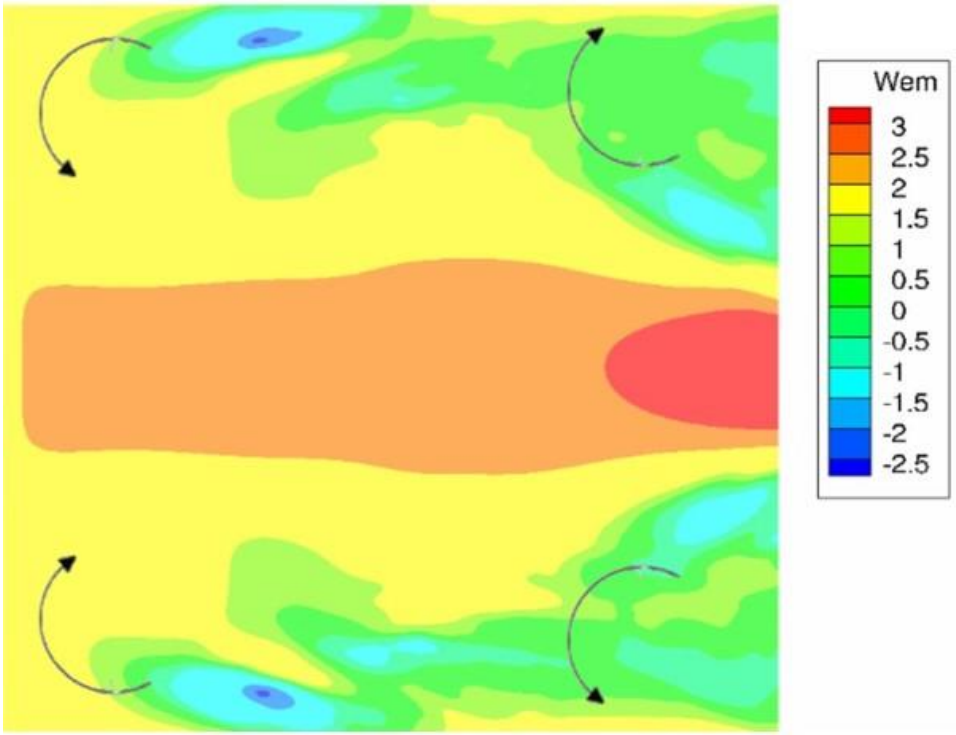

Figure 38: PIV - Velocity field of the quadrotor for d/D=1.7.

7.6.4 General Overview – Diamond

The figures below delineate the velocity fields of the diamond test case at the positive tilt angle for all the various hub distances d/D. The red, yellow and green regions presented the generated upwash, while the pale green and the blue regions the downwash. First of all, it was evident that as the rotor spacings increased the upwash regions were highlighted up until the distance became so distinct that each rotor started to operate almost independently. As seen in almost all figures, an intense downwash was evident right after the retrieving side of the 2nd rotor, which was detrimental for the operation of the 4th rotor's advancing side. As cited above, the optimal performance of the diamond configuration at the positive plane tilt was achieved for the non-overlapping rotor distance d/D=1.44. Its corresponding velocity field has been depicted in Figure 45.

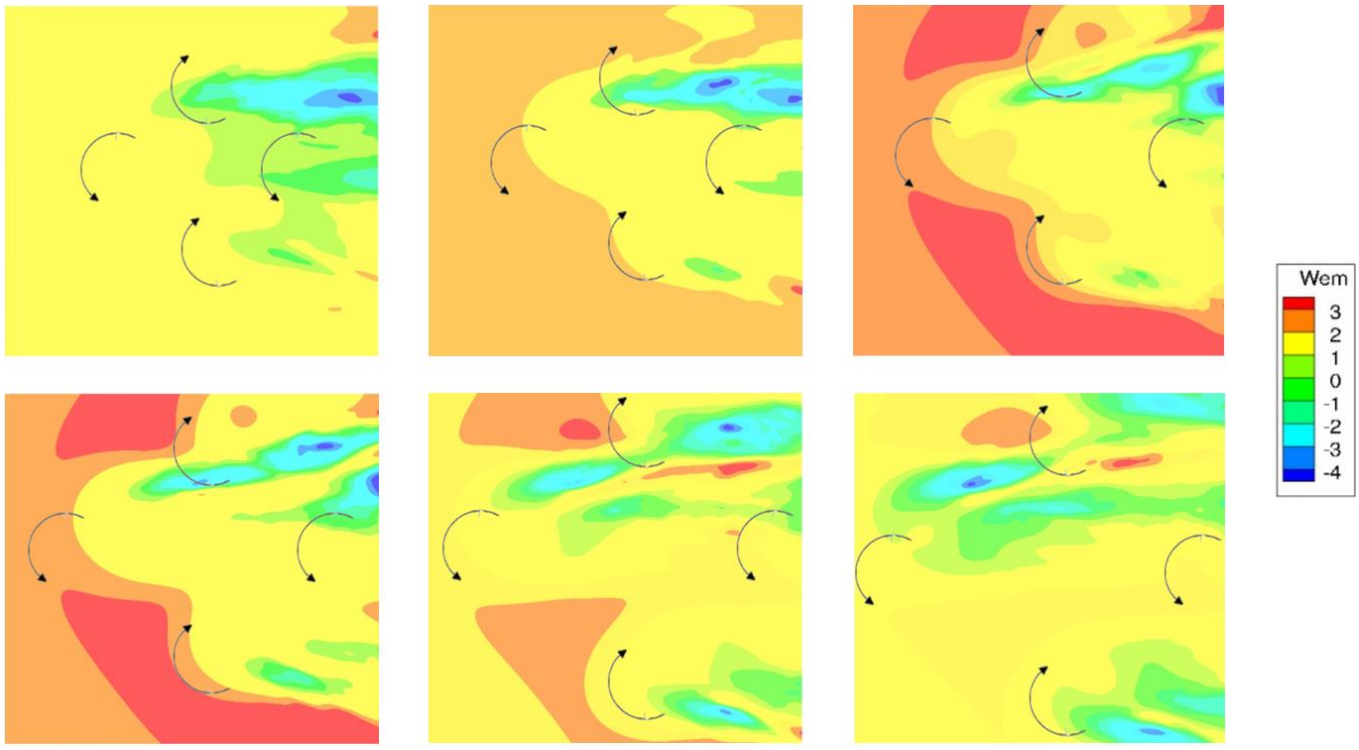

Figure 39: PIV - Velocity field of the diamond test case for increasing d/D.

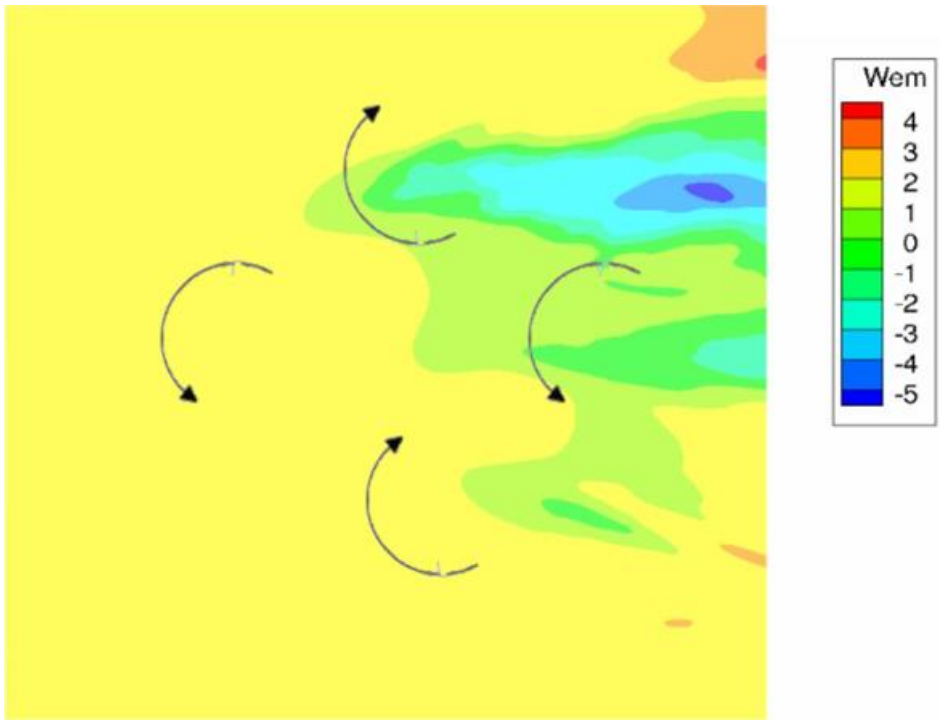

Figure 40: PIV - Velocity field of the diamond test case for d/D=0.74.

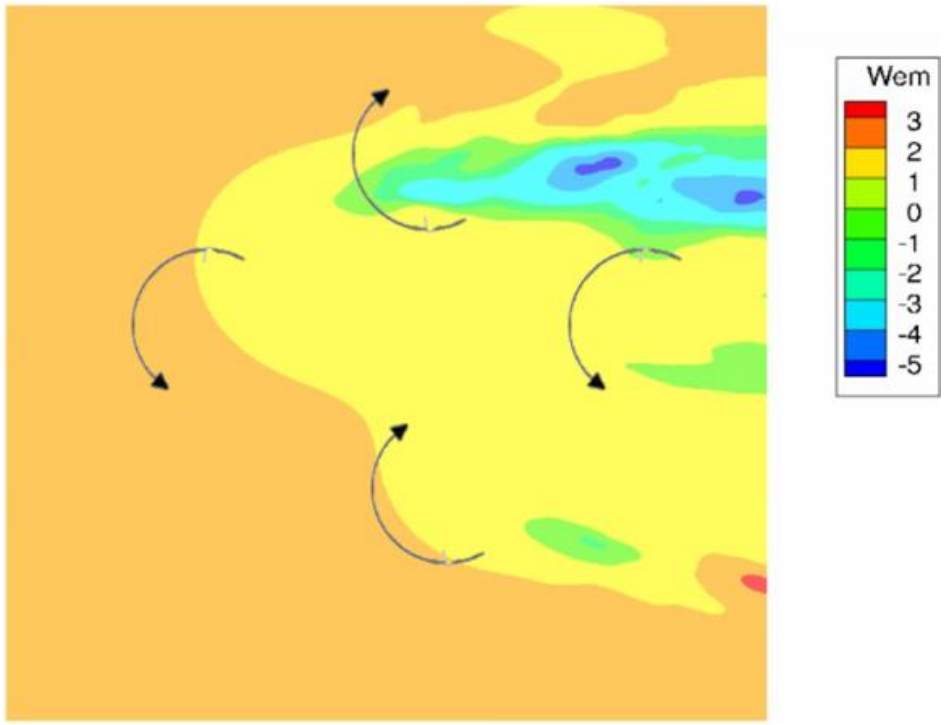

Figure 41: PIV - Velocity field of the diamond test case for d/D=0.84.

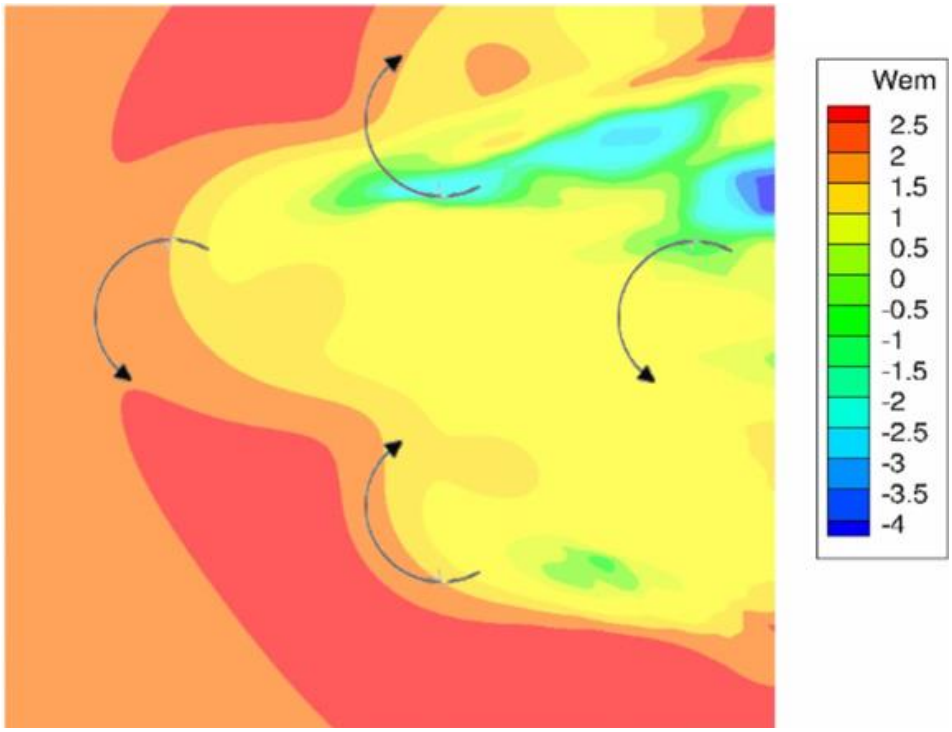

Figure 42: PIV - Velocity field of the diamond test case for d/D=0.96.

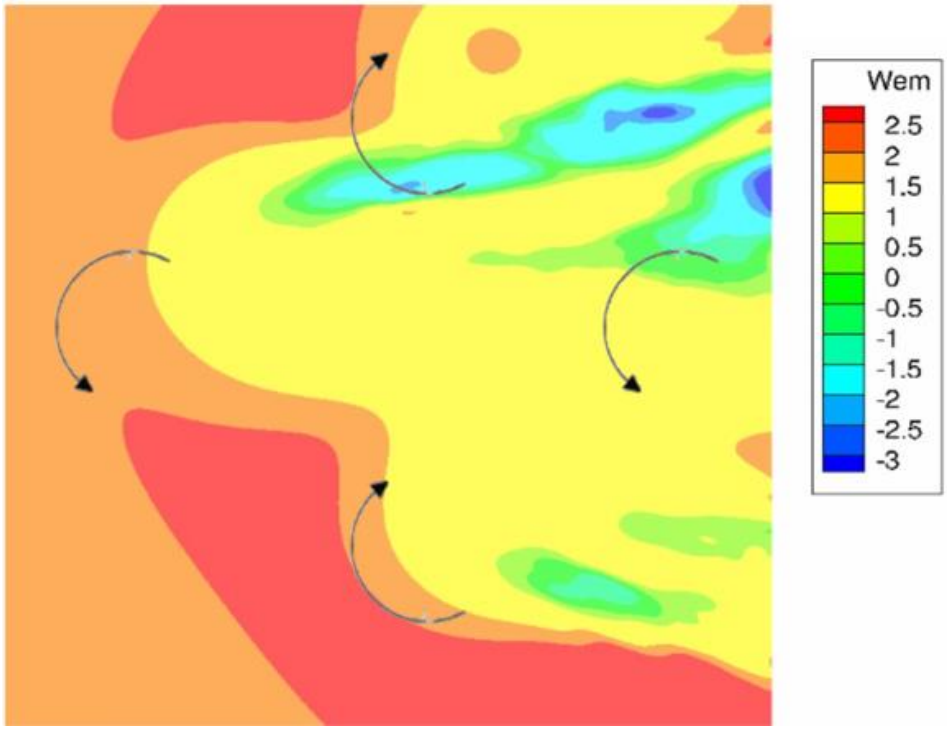

Figure 43: PIV - Velocity field of the diamond test case for d/D=1.

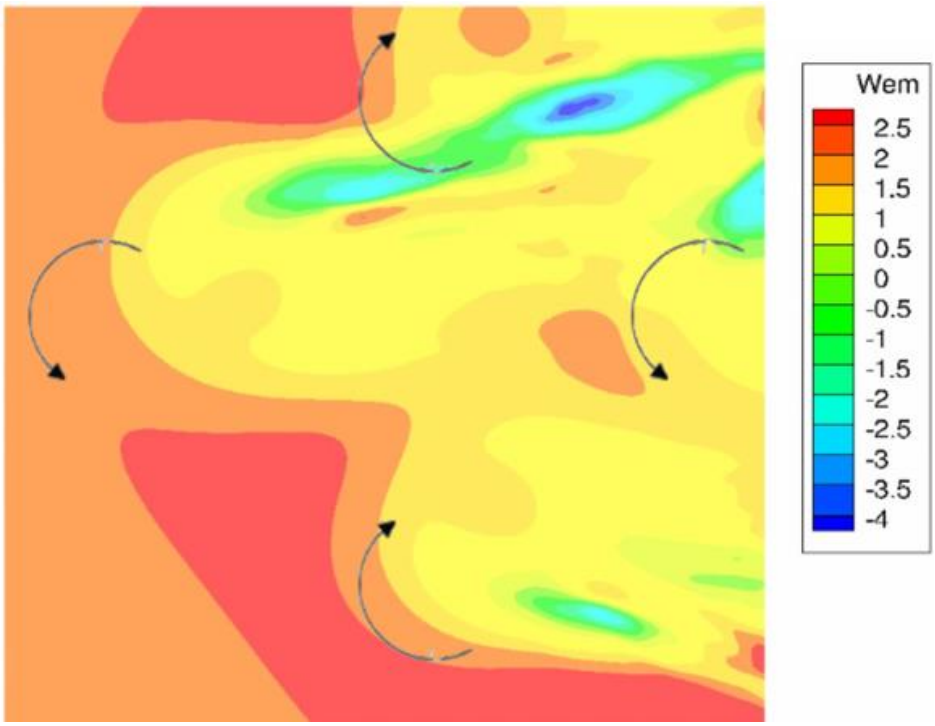

Figure 44: PIV - Velocity field of the diamond test case for d/D=1.22.

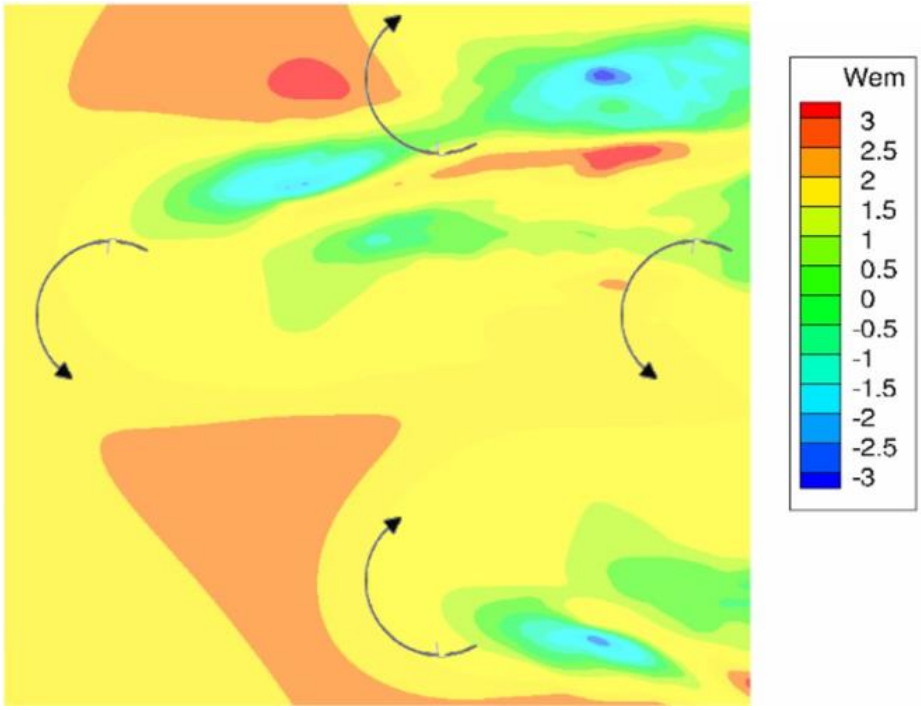

Figure 45: PIV - Velocity field of the diamond test case for d/D=1.44.

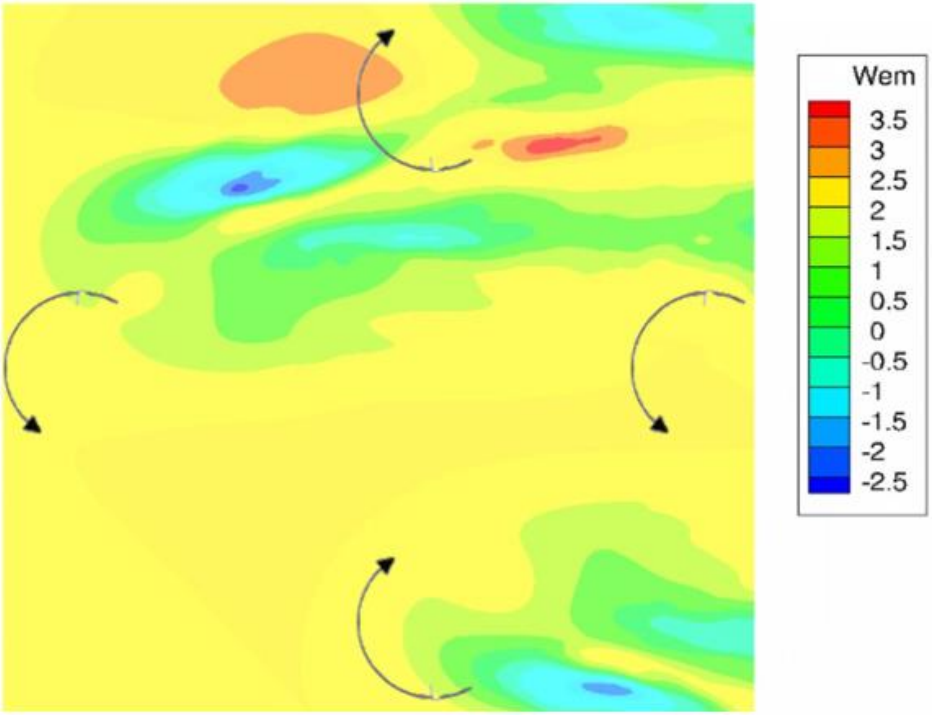

Figure 46: PIV - Velocity field of the diamond test case for d/D=1.7.

8. Discussion

The DLR experiment was also simulated by other universities and institutions through their IN-HOUSE developed codes [3]. CIRA created RAMSYS which was a free-wake lattice boundary element methodology solver, while DLR used UPM (Unsteady Panel Method). ONERA developed PUMA, an assemblage of aerodynamic and kinematic modules (lifting line, free wake and multi-body) and IAG applied its high-fidelity CFD simulation FLOWer. The results of each code have been presented below in comparison to the experimental ones and the thick body data. It is worth noting that the Thick Body method (T.B.) of the CORAL code presented a tremendous resemblance with the UPM code in some cases. Nonetheless, the various profound discrepancies among the different computational tools can be attributed to the way the geometry of tip vortices, and especially the rolled-up ones, were simulated.

Generally, all the codes converged to similar results. Yet, for every test case there was a sole code that digressed remarkably from the experimental data and all the others. For the bearhug and the breaststroke test cases at both a positive and a negative plane tilt, the CORAL presented an overestimation of the aft rotors' torques reaching on average a +5% and a +30% deviation respectively (Figure 47, Figure 48). At the diamond test case, the CORAL acquainted again a prodigious difference, with a magnitude up to +20%, at the 4th rotor's torque for small hub distances and a positive plane tilt. Yet, the UPM's torque for the 3rd rotor diverged even more reaching almost -35% for the same conditions (Figure 49).

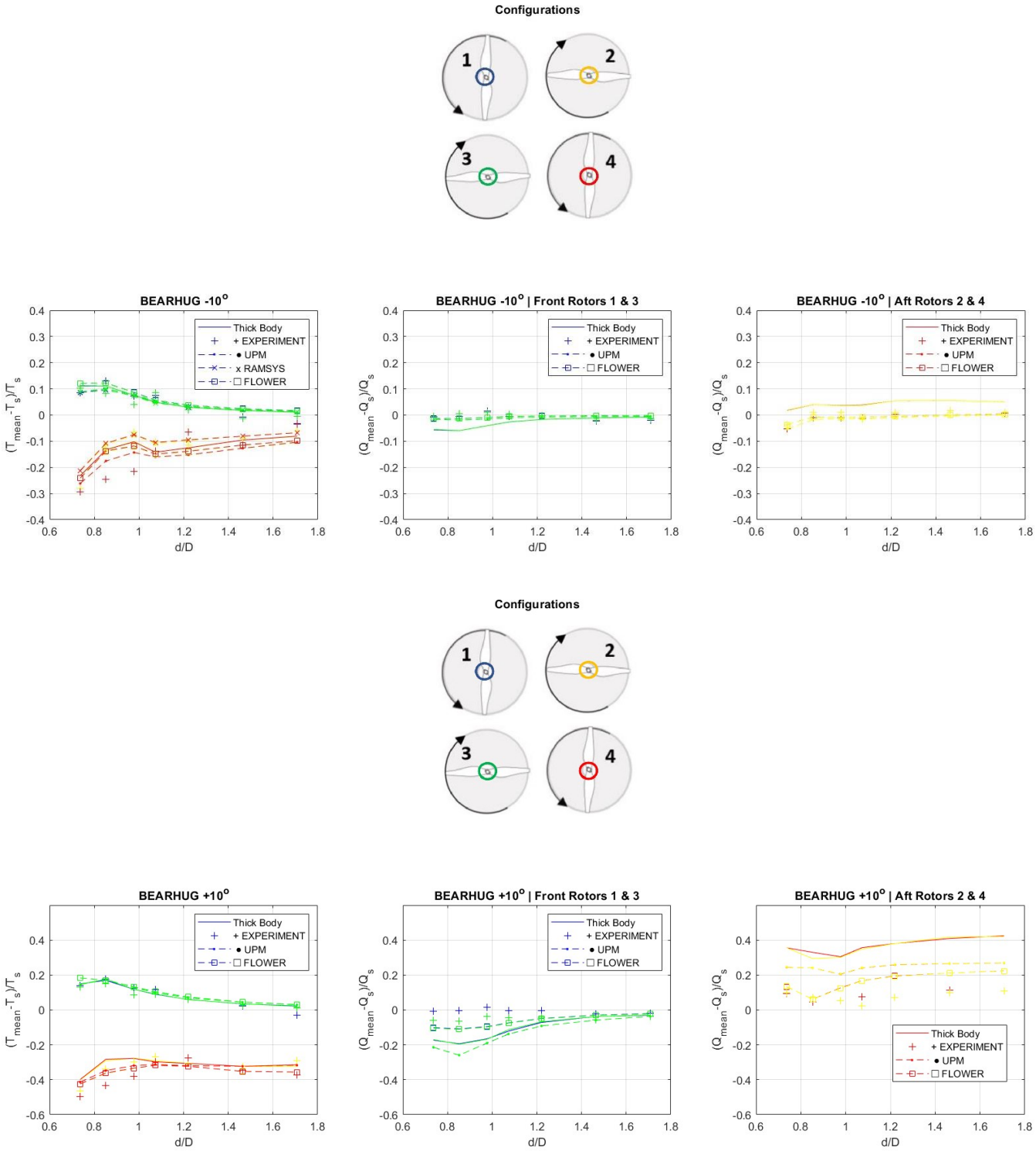

Figure 47: Research Results – Bearhug Configuration – Plane tilt -10°/+10°.

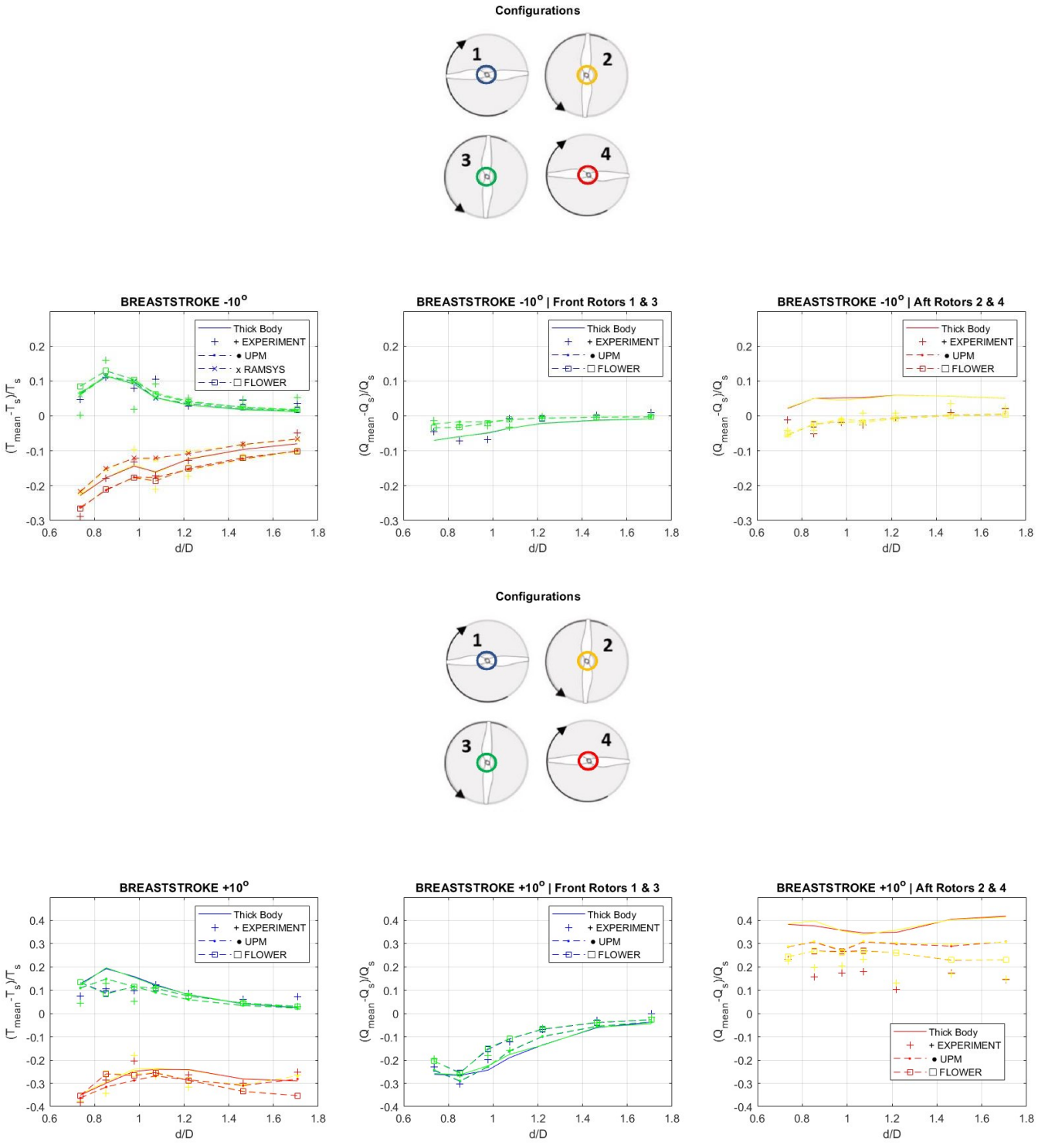

Figure 48: Research Results – Breaststroke Configuration – Plane tilt -10°/+10°.

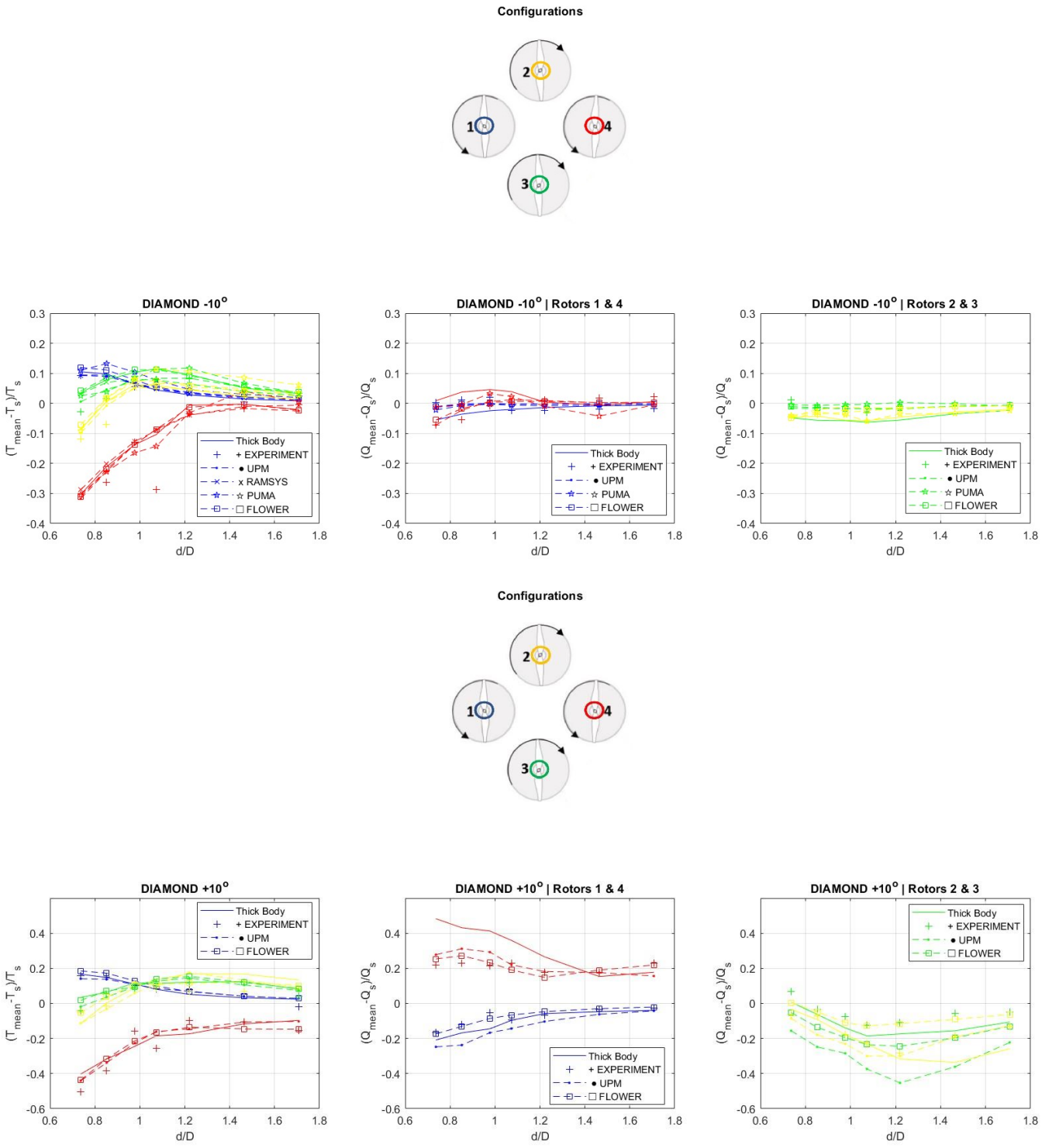

Figure 49: Research Results – Diamond Configuration – Plane tilt -10°/+10°.

9. Conclusions

This thesis was centered around the investigation of the wake interactions between four high-speed rotors in a plus or a cross configuration, while simultaneously their rotor spacing was altered. The three test cases were bearhug, breaststroke and diamond. When convenient, the first two were clustered into a group called square test cases.

Initially, each rotor's thrust and torque were plotted after their normalization with the single rotor's respective quantities. That enabled the local comparison of each of the four rotors individually with a single rotor and aided the notation of numerous remarkable observations about their individual performance. Nonetheless, the four rotors function as a cooperative system and in most cases the results of each rotor contradicted with all the others. Hence, the total rotor sum of each configuration was calculated and collated against the performance of a hypothetical test case that entailed four single rotors that did not interact internally.

Prior to the research, the square test cases seemed the most favorable as they are preferred prodigiously from UAV manufacturers. That perception was confuted after the previously referred contradiction that shed light upon the dominance of the diamond test case, as the only one that aggregately surpassed the performance of the four single rotors. For all the diamond non-overlapping hub distances the total output thrust was higher and required less power than the single rotor test case. The main reason was the operation of the lateral rotors within the first rotor's upwash regions, which were formed by its rolled-up tip vortices. For both a negative and a positive plane tilt and non-overlapping blades ($d/D > 1$), the thrusts augmented over 1%. For the negative rotor plane tilt especially, the maximum proportional enhancement of thrust reached 2.5% for $d/D=1.2$. Additionally, for the negative plane tilt the torque plunged at around 2.5%, regardless of the blades distance.

The square test cases had also encouraging results locally, yet their universal efficiency failed to outstrip the four rotors. Specifically, despite of the extremely beneficial Side-by-Side alignment of the front rotors in the square configurations, the Tandem alignment among the front and the aft rotors impacted significantly the later, as they struggled to operate within the downwash released by the front especially for the non-overlapping and the intense overlapping cases. Nevertheless, rotor hub distances with slightly overlapping blades and negative plane tilt were individually more efficient than the single rotor, as they did not only enhance the performance of the front rotors, but also positively influenced the aft rotors due to the side-by-side interactions that they generated. The most effective hub distancing d/D for both square configurations and a negative plane tilt was 0.96, which accounted for a slight blade overlapping. For the positive plane tilt both square systems exhibited a notable decrease in performance as the rotor spacings widened, while they both demonstrated optimal performance at the overlapping distance of $d/D=0.84$.

It is meaningful to mention that for the sake of this thesis the system's plane rotation was universal with the rotors fixed on it, leaving no margin to rotors for any independent or relative movement. Having this in mind, further research is still required on the vertical unconstrained separation of the front rotors from the aft. The realization of such configurations will delve into more complex wake interactions and it will clarify the fidelity of the results that have been produced by the current investigation. Finally, the cited research findings in conjunction with the proposed researching actions can be vital for the high-speed multicopter industry, since there are scant papers about the optimal rotor configurations and spacings of multicopters.

10. Appendix

10.1 I. CORAL code

The CORAL code (Comprehensive Rotorcraft Analyses Lab) was jointly developed by Roma Tre – RM3 University, National Technical University of Athens-NTUA and Carleton University's Rotorcraft Research Group – CU. CORAL is equipped with various tools for conducting aeroelastic and aero-acoustic analyses on helicopter configurations. The code's aerodynamic component comprises of models with different levels of accuracy, including free wake vortex particle modules and a URANS hybrid CFD module [18], [3]. The choice of module to apply in each analysis depends on the required time efficiency and level of accuracy. The free vortex wake models solve the inviscid-incompressible-unsteady flow equations for lifting/non-lifting bodies treated as lifting lines, lifting surfaces, or thick panel bodies. On the other hand, the CFD module, which is a hybrid of a Eulerian and a Lagrangian model, solves the compressible flow equations on structured and unstructured meshes confined around solid bodies. It is worth noting that the analyses consider both fully resolved and actuator line representations of lifting bodies.

11. References

[1] Wikipedia, "Bell UH-1 Iroquois," 2006.

[2] Wikipedia, Sikorsky S-97 Raider, 2015.

[3] L. L. T. Z. G. B. V. e. a. R. Boisard, "Rotor / Rotor aerodynamic interactions – A Garteur Action Group," Sweden, 2022.

[4] V. N. J. D. A. D. A. D. Lauriane Lefevre, "Experimental velocity fields evaluation of the rotor/propeller interactions for high-speed helicopters with different propeller positions," 2022.

[5] J. G. J.-C. M. A. Le Pape, "Experimental Investigations of Rotor-Fuselage Aerodynamic Interactions," in *30th European Rotorcraft Forum*, Marseille, France, 2004.

[6] A. B. S. J. Y. Y. B.G. van der Wall, ""“Semi-Empirical Physics-Based Modeling of FuselageRotor and Fuselage-Wake Interferences for Comprehensive Codes," in *70th Annual Forum of the American Helicopter Society*, Montreal, Canada, 2014.

[7] R. B. P. B. B. R. R. G. B. K. F. B. A. V. A. Filippone, "Helicopter Wakes in Confined Spaces, including Ground Effect," in *37th European Rotorcraft Forum, Vergiate and Gallarate*, Vergiate and Gallarate, Italy, 2011.

[8] M. P. G. K. Y. M. Ramasamy, "Measurements to Understand the Flow Mechanisms Contributing to Tandem-Rotor Outwash," in *71th Annual Forum of the American Helicopter Society*, Virginia Beach, USA, 2015.

[9] R. E. B. Timothy M. Fletcher, "Main Rotor-Tail Rotor Interaction and Its Implications for Helicopter Directional Control," *Journal of the American Helicopter Society,* 2008.

[10] M. V. A. K. E. K. F. K. a. Z. V. K. Christodoulou, "Aerodynamic Analysis of a Quadcopter Drone Propeller with the Use of Computational Fluid Dynamics," 2019.

[11] H. N. L. Z. X. W. M. Z. He Zhu, "Design and assessment of octocopter drones with improved aerodynamic efficiency and performance," 2020.

[12] N. K. Dhwanil Shukla, "Multirotor Drone Aerodynamic Interaction Investigation," 2018.

[13] M. Ramasamy*, "Measurements Comparing Hover Performance of Single,," NASA Ames Research Center, Moffett Field, CA, 2013.

[14] L. A. J. Bain Lawrence J., "INVESTIGATION OF COMPOUND HELICOPTER AERODYNAMIC

INTERFERENCE EFFECTS," 1967.

[15] C. G. M. E. B. B. B. B. E. W. M. W. S. Patrick O. Bowles, "A Model-Scale Wind-Tunnel Study of Main Rotor/Propeller Interference," in *72nd AHS annual forum*, West Palm Beach, Florida, 2016.

[16] A. A. Kostek, "Experimental Investigation of Quadrotor Aerodynamics with Computational," German Aerospace Center (DLR), Gottingen, Germany, 2023.

[17] G. P. N. S. F. N. C. S. R. L. M. G. G. B. c. S. F. P. A. S. D. H. M. R. Vasilis Riziotis, "A NEW COMPREHENSIVE ANALYSIS TOOL FOR THE PRELIMINARY DEISGN AND DESIGN EVALUATION OF HELICOPTERS - THE CORAL PROJECT," 2019.

[18] G. P. N. S. V. Riziotis, "GenUVP: Input/Output description," 2019.

[19] Istitute of Risk Management, "About Ris Management, Institute of Risk Management," Institute of Risk Management - IRM, 2016. [Online]. Available: https://www.theirm.org/about/risk-management. [Accessed 6 2 2017].

[20] A. Kostek, "AG 25: Rotor – Rotor Wakes Interactions," 2022.

.

Αεροδυναμική Αλληλεπίδραση Δρομέων

Ζιάβρας Χρήστος

Αθήνα 2023

--- End of Document ---